Geomorphology 350 (2020) 106908

Contents lists available at ScienceDirect

Geomorphology

journal homepage: www.elsevier.com/locate/geomorph

Regional relative tectonic activity of structures in the Pampean flat slab segment of Argentina from 30 to 32°S

Jeremy M. Rimando[a,b,*], Lindsay M. Schoenbohm[a,b]

[a] Department of Earth Sciences, University of Toronto, Toronto, Ontario M5S 3B1, Canada
[b] Department of Chemical and Physical Sciences, University of Toronto Mississauga, Mississauga, Ontario L5L 1C6, Canada

ARTICLE INFO

Article history:
Received 24 April 2019
Received in revised form 9 October 2019
Accepted 11 October 2019
Available online 31 October 2019

Keywords:
Geomorphic indices
Relative tectonic activity
Pampean flat slab segment
Strain distribution

ABSTRACT

The Pampean flat slab segment of the Central Andes in Argentina is a broad, active deformation zone subject to both plate boundary-related and intraplate deformation. To the west, plate boundary-related deformation is dominated by thin-skinned fold-and-thrusts of the Precordillera, while to the east, intraplate deformation involves thick-skinned reverse faults of the Sierras Pampeanas. GPS data and absolute dating of displaced geomorphic features suggest that most of the active permanent deformation occurs between these two regions at the Andean orogenic front and that there is a west-to-east trend of decreasing shortening rates. However, GPS stations and sites with geomorphic slip rate measurements are currently too sparse and cover too short a time period to make reliable inferences about the longer-term distribution and relative rates of deformation. Mountain range-scale geomorphic indices, on the other hand, reflect tectonic activity since at least the Pleistocene. In this study, we measured geomorphic indices (hypsometric integral and curves, basin elongation ratio, basin volume-to-area-ratio, valley floor width-to-height ratio, mountain front sinuosity, and normalized steepness indices of rivers) from 10 different N-S striking, range-bounding faults that span both the Precordillera and Sierras Pampeanas regions from west to east. We use these data to assess the regional relative tectonic activity of major Quaternary deformation features in the Pampean segment of the Central Andes. Even when variations in climate and geology are considered, mean values for each geomorphic index suggests uplift rates for the 10 mountain-range bounding faults display local trends that are closely associated with the structural style and tectonic evolution of these structures. Although vertical uplift rates vary little, horizontal shortening rates are higher for the Precordillera fold-and-thrusts in the west than the thick-skinned reverse faults of the Sierras Pampeanas in the east, due to shallower fault dips for Precordilleran structures. The similarity with decadal slip rate gradients from GPS studies could possibly indicate that the stress-field has been constant since at least the Pleistocene, but further slip rate studies over broader time intervals in the late Quaternary are necessary to confirm this. Variations observed in relative uplift rates along each fault point to sites that warrant further detailed study of slip rates and evaluation of associated seismic hazards.

1. Introduction

Tectonic shortening of the South American plate results from the east-directed convergence of the Nazca plate causing Neogene crustal thickening in the Central Andes (Allmendinger et al., 1997; Isacks, 1988; Kley and Monaldi, 1998; Ramos, 1988; Ramos et al., 1996, Sempere et al., 1990; Sheffels, 1990), a region which has one of the thickest continental crusts (>70 km) on Earth (Wigger et al., 1994; Zandt et al., 1994; Mcquarrie et al., 2005; Giambiagi et al., 2012). In the Pampean flat slab segment, north-south trending thrust and reverse faults in the upper plate accommodate east-directed plate convergence (Ramos, 1988; Ramos et al., 1998; Ramos et al., 2002, 2004; Ramos and Folguera, 2009). These thrust and reverse faults, which are almost entirely associated with mountain range fronts, are widely distributed, extending as far as 700 km east from the plate boundary, and are responsible for most of the relief in back-arc region of the Pampean flat slab. In contrast, the horizontal GPS velocity field and narrow longitudinal distribution of documented Quaternary-active faults and shallow crustal seismicity have led previous workers to suggest highly-localized back-arc active deformation, which possibly defines a microplate

* Corresponding author at: Department of Earth Sciences, University of Toronto, Toronto, Ontario M5S 3B1, Canada.
E-mail address: jeremy.rimando@mail.utoronto.ca (J.M. Rimando).

https://doi.org/10.1016/j.geomorph.2019.106908
0169-555X/

between the Nazca and South American plates (Brooks et al., 2003, and references therein).

The coverage and resolution in space and time of the geodetic, seismic, and neotectonic observations suggesting localized deformation, however, are currently too limited to definitively rule out more widely-distributed, active deformation throughout the back-arc contractional wedge. For instance, the continuous GPS station network in the Andes is not dense enough to measure slip rates on individual faults and can only reliably describe deformation on a decadal timescale. On the other hand, neotectonic and paleoseismic slip rates, which cover much longer time scales than GPS (late Pleistocene to Holocene), are site-specific and usually not available for all structures within a large region. Indeed, the rarity in studies employing Quaternary geochronology has limited the characterization of the activity of most of the structures in the Precordillera and the Sierras Pampeanas (Costa et al., 2015a, and references therein). Knowledge of the longer-term distribution and rates of movement of major structures in the region will provide a better understanding of the dominant controls on ongoing mountain building, partitioning of strain, and the relative amounts of crustal deformation accommodated by end-member thrust tectonic styles.

One approach for filling the spatio-temporal data gap in the Pampean flat slab segment of the Andes is measurement of geomorphic indices on fault-bounded mountain range fronts. Morphometric measurement allows for broader spatial coverage (hundreds of kilometers) and increased temporal coverage due to longer required response times (into the Pleistocene) and is, therefore, appropriate for addressing questions about longer-term deformation (Bull, 2008; Burbank and Anderson, 2012). Geomorphic indices, dimensional ratios of a landform (or its parts), can be used to quantify the amount of modification the landform has undergone over thousands to millions of years and to analyze the relative contributions of tectonics, climate, and geology to shaping that landform. Sensitive to the balance between active tectonics and surface processes, geomorphic indices can be used to determine relative level of tectonic activity of an area, as long as the possible influence of climatic and lithologic conditions on these indices are accounted for (Bull, 2008; Bull and McFadden, 1977; Burbank and Anderson, 2001; Cyr et al., 2010; Keller and Pinter, 2002; Kirby et al., 2003; Kirby and Whipple, 2012; Rockwell et al., 1985; Snyder et al., 2000; Wobus et al., 2006). Various combinations of geomorphic indices have been successfully employed in studying relative tectonic activity of large regions worldwide (e.g., Bull and McFadden, 1977; Rockwell et al., 1985). Despite the extensive use of different combinations of geomorphic indices for regional relative tectonic activity analysis in other orogens, these techniques have only been applied locally in this part of the Andes, in a study in which river longitudinal profile analysis on the ranges of the easternmost Sierras Pampeanas were used to determine relative uplift rates (Canelo et al., 2019). However, no regional study has been done yet in the seismically active Pampean flatslab region of West-Central Argentina in the context of assessing regional strain distribution patterns.

The aim of this study is to explore the degree and trend of variations in relative uplift rate along major active faults that span the Pampean flat slab segment of the Andes (30–32°S) and explore possible trench perpendicular (W-E) gradients in relative uplift and shortening rates that may provide information on the relationships among slab-dip, structural style, and tectonic evolution of structures to the observed strain distribution. Our secondary aim is to identify priority sites that may require quantitative slip-rate determination and more detailed studies of seismic hazard potential. We accomplish this by using a combination of range front- and drainage basin-based geomorphic indices to characterize the spatial distribution of relative uplift rates on 10 nearly parallel, north-south oriented faults that reach as far as ~700 km east of the Peru–Chile Trench.

2. Background

2.1. Tectonic setting

2.1.1. Regional tectonics

The Pampean flatslab segment (Fig. 1), a section of the Nazca plate from 27 to 33 °S that is subducting beneath the South American plate at an unusually shallow angle, is characterized by a convergence rate of 6.3 cm/yr (Brooks et al., 2003; Kendrick et al., 2003). It is associated with a broad zone of plate boundary-related and intraplate deformation that reaches more than 700 km east of the Peru-Chile trench (Gutscher et al., 2000). Seismic and tomographic data demonstrate that the slab reaches as far as 300 km east into the continental interior at a depth of only ~100 km (Cahill and Isacks, 1992; Engdahl et al., 1998; Gutscher et al., 2000; and Smalley et al., 1993), likely the result of subduction of the Juan Fernandez Ridge (Pilger, 1984; von Huene et al., 1997v).

East-directed flat-subduction produced nearly north-south oriented thrust and reverse faults in the upper plate (Ramos, 1988; Ramos, 1998; Ramos et al., 2002, 2004; Ramos and Folguera, 2009) (Figs. 1–3). Most of the permanent deformation taking place at these latitudes is divided into two, oppositely-verging thrust systems in the back-arc region: 1) the predominantly west-dipping, thin-skinned Precordillera fold-and-thrust belt (plate-boundary related deformation) in the west, and 2) the predominantly east-dipping, thick-skinned, Sierras Pampeanas basement uplifts (intraplate deformation) in the east.

Plate boundary-related deformation migrated eastward through time and reached the Eastern Precordillera at ~2.6 Ma, while intraplate deformation in the Sierras Pampeanas propagated westward, beginning at its easternmost reach at ~6–5.5 Ma and arriving in the west, at Pie de Palo, at around ~3 Ma (Jordan et al., 1983a, 1983b; Jordan and Gardeweg, 1989; Jordan et al., 1993; Ramos, 1988; Ramos et al., 2002; Zapata and Allmendinger, 1996). At present, an ~50 km wide band of Quaternary-active deformation called the Andean Orogenic Front is located between the oppositely-verging Precordillera and Sierras Pampeanas regions (Brooks et al., 2003; Costa, 1999; Fielding and Jordan, 1988; Groeber, 1944; Kadinsky-Cade et al., 1985; Meigs et al., 2006; Ramos et al., 1997; Siame et al., 2002; Siame, 2005; Siame et al., 2015; Smalley et al., 1993; Uliarte et al., 1987; Vergés et al., 2007). Highly-localized deformation along the Andean Orogenic Front is indicated by GPS gradients, spatial clustering of high-magnitude, shallow (5–35 km) crustal earthquakes (Smalley and Isacks, 1990; Cahill and Isacks, 1992; Smalley et al., 1993; Engdahl et al., 1998; Gutscher et al., 2000), and documentation of almost 90 % of Quaternary deformation in this strip (Cortés et al., 1999; Costa et al., 2000, 2006, and references therein) (Fig. 2). GPS estimates of back-arc deformation rates between the Eastern Precordillera and the Western Sierras Pampeanas range from 2 to 7 mm/yr (Kendrick et al., 2006; Kendrick et al., 1999, 2001, 2003; Brooks et al., 2003). Brooks et al. (2003) explains strain localization by proposing that a doubly-vergent microplate, located between the Nazca and South American plates, accommodates deformation mainly at its boundaries rather than across the entire back-arc region.

2.1.2. Precordillera and Sierras Pampeanas structures

Most mapped major structures in the predominantly thin-skinned Precordillera region, such as the Eastern Sierra del Tigre (ETF), Eastern Sierra de la Cantera Fault (ECF), and the Sierra de Osamentas Fault (OF), dip to the west at a shallow angle (Fig. 3). These generally dip ~40°, but reach up to 60° in westernmost Pre-

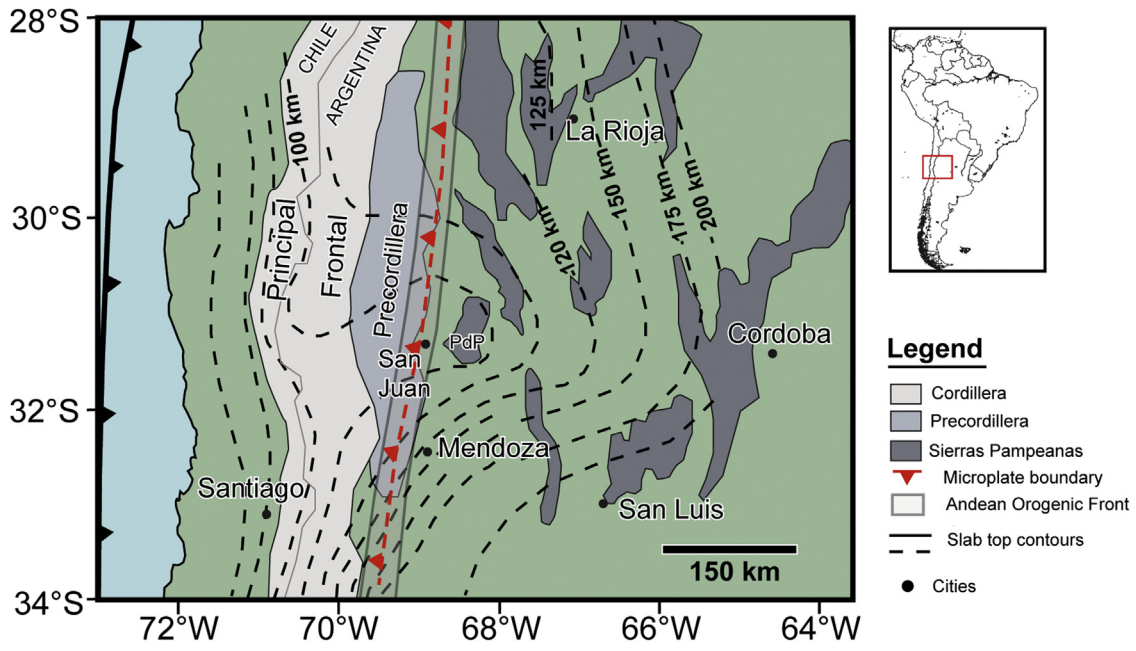

Fig. 1. A map of the Pampean flat slab segment showing the extent of the top of the subducting slab (dashed black lines) by Anderson et al. (2007) and Mulcahy et al. (2014).

cordillera where earlier-formed imbricate thrusts are progressively steepened (Von Gosen, 1992). Although less common, east-dipping structures such as the Morados-Villicum-Zonda-Pedernal Faults (MVZPF) are found in the east at the boundary with the Sierras Pampeanas (Fig. 3; Von Gosen, 1992; Ragona et al., 1995; Ramos and Vujovich, 2000; Cardó and Díaz, 2005). The contrasting vergence of the MVZPF could reflect its origin as a backthrust related to an east-verging, blind crustal wedge (Vergés et al., 2007) or could possibly mark the onset of thick-skinned mode of deformation (Von Gosen, 1992). Late Quaternary activity has been documented in close proximity to each of these range-bounding Precordilleran structures in the form of parallel scarps cutting across alluvial fans (Bastias, 1985; and Siame et al., 1997, 2002; Millán & Perucca, 2011; Perucca and Onorato, 2011; Rockwell et al., 2014; Perucca et al., 2015; Lara et al., 2018; and Rimando et al., 2019; Fig. S2–13).

Opposite to what is observed in the Precordillera, structures in the thick-skinned Sierras Pampeanas, such as the Western Pie de Palo Fault (WPF), Valle Fertil Fault (VF), Pocho Fault, and Sierra Chica Fault Zone (SCFZ), are predominantly steeply east dipping, with only a few structures that are west dipping, such as the Eastern Pie de Palo Fault (EPF) and the Sierras de los Llanos & Sierras de las Minas y Ulapes Faults (LMUF) (Fig. 3). Most faults dip at least ~60° and can reach nearly vertical (Guerrero et al., 1993; Ragona et al., 1995; Furque et al., 1998; Vujovich et al., 1998; Bonalumi et al., 1999; Caselli et al., 1999; Ramos and Vujovich, 2000; Candiani et al., 2001; and Bellahsen et al., 2016). The steep dip of these faults is attributed to reactivation of normal faults related to Triassic rifting (Ramos et al., 2002, and references therein). Late Quaternary activity is also documented along most structures in this region through observation of recent scarps, range morphology, and recent seismicity (Kadinsky-Cade et al., 1985; Regnier et al., 1992; Zapata, 1998; Costa et al., 2000; Costa et al., 2001a, 2001b, 2001c; Richardson et al., 2013; Costa et al., 2014; Ortiz et al., 2015; Siame et al., 2015; Bellahsen et al., 2016; Rothis et al., 2018; Fig. S2–13). There are a few structures, however, such as the Sierras de los Llanos & Sierras de las Minas y Ulapes Faults (LMUF) and the Western Pie de Palo Fault (WPF), which have not been associated with recent deformation features, and whose activity has yet to be determined.

2.2. Lithology

Lithological variation can lead to differences in rock erosional resistance and can therefore affect measurement of geomorphic indices (Moglen and Bras, 1995; Kühni and Pfiffner, 2001, and references therein). Due to the scale of the study area, we were unable to measure the determinants of rock erodibility directly in the field. Rather, we followed previous work that infer erosional resistance from rock type (e.g., Lifton and Chase, 1992; Lague et al., 2000; Kühni and Pfiffner 2001; Korup, 2008; Jansen et al., 2010). We use a compiled geologic map (Fig. 4a) and follow the same erodibility ranking from studies that conducted in-situ tests in different tectonic and climatic settings (e.g. Selby, 1980; Clayton and Shamoon, 1998) to create a rock erosional resistance map (Fig. 4b). The thin-skinned structures of the Precordillera fold-and-thrust belt in the west developed on an Early Paleozoic sequence of carbonate and siliciclastic shallow marine (inner and outer continental shelf), and siliciclastic deep marine rocks, and proximal foreland, fluvial and glacial continental, and synorogenic deposits. In contrast, the thick-skinned reverse faults of the Sierras Pampeanas in the east cut through Precambrian–Early Paleozoic metamorphic and igneous rocks that are partially covered by a series of Late Paleozoic continental clastic fluvial, alluvial, and glacial deposits (Bonalumi et al., 1999; Candiani et al., 2001, 2010; Cardó and Díaz, 2005; Costa et al., 2001a; Costa et al., 2001b; Fauqué et al., 2004; Furque et al., 1998; Miró et al., 2005; Ragona et al., 1995; Ramos and Vujovich, 2000; Ramos, Caminos, et al., 2000; Ramos et al., 2010; Vujovich et al., 1998).

2.3. Geomorphology

The landscape of the Pampean flat slab from 30–32 °S is characterized by north-south-trending parallel mountain ranges, reflecting the contemporaneous east-directed shortening in the region. The ranges in the Precordillera, which are narrower compared to ranges in the Sierras Pampeanas, are an expression of stacked Paleozoic sedimentary thrust sheets separated by similarly narrrow, highly-deformed intermontane basins (Suriano et al., 2015). Ranges of the Sierrras Pampeanas, on the other hand, are wider with highly assymetrical profiles with a steep fault-bounded

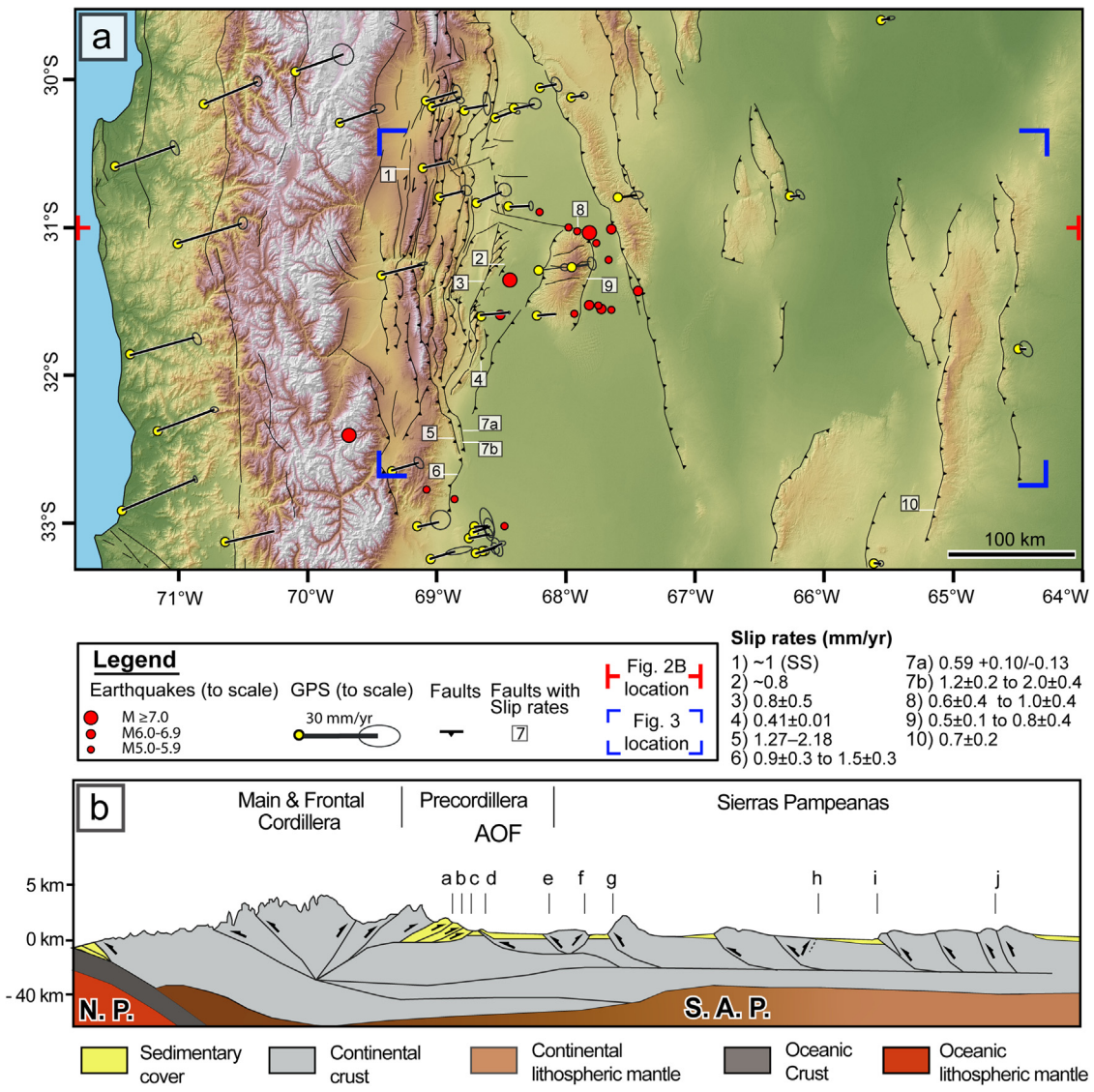

Fig. 2. Tectonic features (Costa et al., 2000 and Siame et al., 2002), seismicity (Engdahl and Villaseñor, 2002), GPS velocity field (Brooks et al., 2003), and Quaternary slip rate data (Costa et al., 2015a, 2015b; Costa et al., 2018; Rimando et al., 2019; Rockwell et al., 2014; Salomon et al., 2013; Schmidt et al., 2011; Schoenbohm et al., 2013; and Siame et al., 2002, 2006, 2015) in the Pampean flat slab segment plotted on a 30-meter ASTER digital elevation model. The red perpendicular symbols indicate the location of the cross-section in Fig. 2B. The blue corners show the location of Fig. 3. Numbers in white boxes indicate faults with known slip rates: 1—El Tigre Fault, 2—La Laja Fault 3—Las Tapias segment of Villicum-Zonda- Pedernal Thrust, 4—Las Higueras 5—La Cal Thrust, 6— La Rinconada Fault Zone, 7a&b— Las Peñas Thrust, 8—Northern Sierra Pie de Palo Fault, 9— Southern Sierra Pie de Palo Fault, and 10— Los Molinos branch of the Comechingones (modified after Rimando et al., 2019). b) Schematic structural cross-section through the Pampean flat slab at 31 °S. Letters indicate faults investigated in this study: a—Eastern Sierra del Tigre Fault. b— Eastern Sierra de Cantera Fault. c—Sierra de Osamentas Fault. d— Morados-Villicum-Zonda-Pedernal Faults. e— Western Pie de Palo Fault. f— Eastern Pie de Palo Fault. g— Valle Fertil Fault. h— Sierras de los Llanos and Sierras de las Minas y Ulapes Fault. i— Pocho Fault. j— Sierra Chica Fault Zone.

side and a gentler hindside, which is reflective of an underlying listric fault geometry (Jordan and Allmendinger, 1986). Intervening basins in the Sierras Pampeanas are wider and largely undeformed. Elevation and relief is generally higher in the Precordillera, with Cerro Pircas as its highest peak standing at 4380 masl, compared to the Sierras Pampeanas, with Mogotes Corallitos as it highest peak standing only at 3032 masl. Ranges in the Precordillera are mostly shorter, due to shorter associated fault segments and/or due to passage of transverse rivers that drain the Principal and Frontal cordillera to the west. On the fault bounded sides of mountain ranges in both regions, piedmonts are composed of extensive contiguous Quaternary alluvial fans which manifest indications of recency of movement (e.g., fold and/or fault scarps) and relative rates of activity of the main range-bounding structures (e.g., outline of outcropping bedrock). Drainage basins of the fault-bound sides of ranges, which generally drain west or east (except in localities where drainage is controlled by planes of weakness, such as jointing and bedding planes) (Fig. S1), can also be parametrized to use as indicators of relative rates of uplift.

2.4. Climatic setting

We use Tropical Rainfall Measuring Mission (TRMM)-based precipitation data to provide additional context for interpreting regional trends in geomorphic indices values, since it is known that climatic differences can control the rates and patterns of landscape evolution (Bookhagen and Strecker, 2012), and consequently, the geomorphic indices used as indicators for relative tectonic activity (Tucker, 2004; Molnar et al., 2006; Attal et al., 2011). In particular, we use the average annual rainfall TRMM data gathered over a span of 12 years (1998–2009). There is no substantial latitudinal precipitation rate gradient between 30–32 °S latitudes (Bookhagen

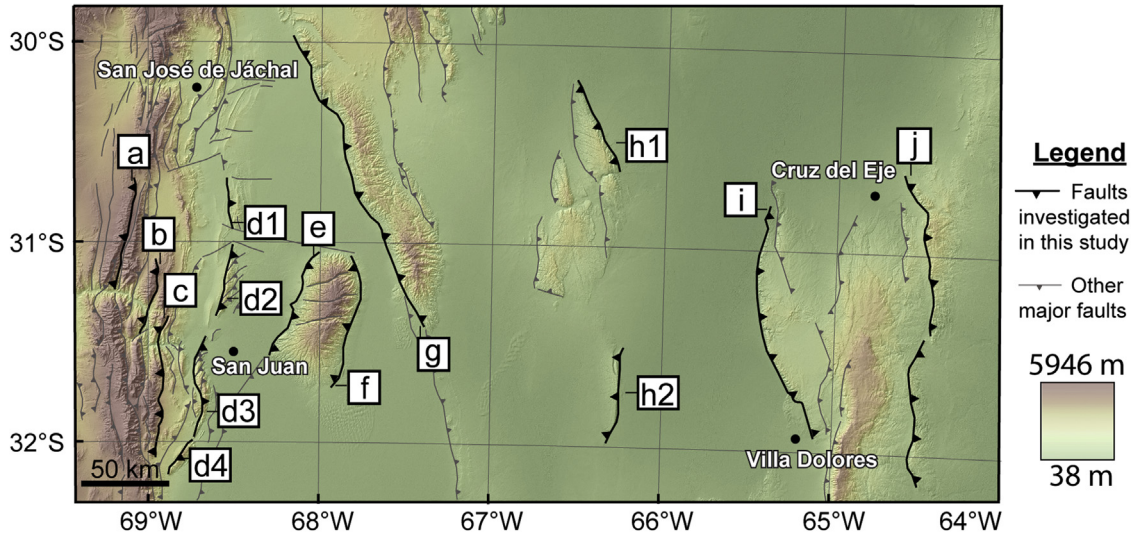

Fig. 3. Fault location map. a—Eastern Sierra del Tigre Fault. b— Eastern Sierra de Cantera Fault. c—Sierra de Osamentas Fault. d1-d4— Morados-Villicum-Zonda-Pedernal Fault. e— Western Pie de Palo Fault. f— Eastern Pie de Palo Fault. g— Valle Fertil Fault. h1-h2— Sierras de los Llanos and Sierras de las Minas y Ulapes Fault. i— Pocho Fault. j— Sierra Chica Fault Zone.

and Strecker, 2012; Fig. 4c). However, longitudinal precipitation rates range from less than 10 mm/yr in the west to as much as 2250 mm/yr in the east. According to the Köppen–Geiger climate classification system, the climate group of the area varies from arid (steppe & dessert) in the west, to temperate in the east (Peel et al., 2007). This considerable west-east climatic gradient can be explained both by a rainshadow effect of the Andean range on the Pacific winds from the west and the gradual loss of moisture from Atlantic winds at they cross the extensive continent from east to west (Bruniard, 1982; Abraham de Vázquez et al., 2000; Houston and Hartley, 2003). This climate has likely been stable since Late Miocene. Paleocosmogenic dating-based erosion rates in the Precordillera (at around 31.25 °S and between 68–69 °W) indicate that areas which are currently receiving low mean annual precipitation (Fig. 4C) were arid since Late Miocene (Amidon et al., 2017). Similarly, in the Late Quaternary, between 31–32 °S and 66.5–68 °W, dating of dune field deposits show repeated reactivation, with the last reactivation taking place ~400–600 years ago. South of our study area (at around 34 °S and between 65–66 °W), but still within regions mapped as having low mean annual precipitation with TRMM, dating of sand dune fields indicate repeated activation between 33–20 ka (Tripaldi and Forman, 2007). This consistency on different timescales allows us to use TRMM-based rainfall data to represent long-term average precipitation gradients.

3. Methodology

We chose 10 nearly parallel, north-south oriented faults that span the study region to measure range front- and drainage basin-based geomorphic indices in order to characterize the spatial distribution of relative uplift rates. From west to east, the faults we examined are: Eastern Sierra del Tigre Fault, Eastern Sierra de Cantera Fault, Sierra de Osamentas Fault, Morados-Villicum-Zonda-Pedernal Fault, Western Pie de Palo Fault, Eastern Pie de Palo Fault, Valle Fertil Fault, Sierras de los Llanos and Sierras de las Minas y Ulapes Fault, Pocho Fault, and the Sierra Chica Fault Zone (Figs. 2 and 3). Characterization of along-strike relative uplift rate variation allows us to infer the structural evolution of individual faults, identify priority sites for future detailed seismic hazard studies, and to see potential sources of uncertainty in data in our regional analysis of relative uplift rates. Analysis of variation among the different structures allows us to examine W-E trends in deformation.

We measured hypsometric Integral (HI), elongation (R_e), volume-to-area ratio (R_{VA}), valley-floor-width-to-height (V_f) ratio, mountain front Sinuosity (S_{mf}), normalized channel steepness index (k_{sn}), and the statistical moments of the hypsometric curve: skewness (Sk), Kurtosis (Kur), Density Skewness (Dsk), and Density Kurtosis (Dkur). This combination of geomorphic indices measured both along and within mountain ranges that span the Pampean flat slab region allow us to detect landform changes related to local tectonic base-level fall associated with range-bounding faults rather than base-level fall related to regional, long wavelength uplift. The widely used mountain front sinuosity (S_{mf}) and valley-floor-width-to-height (V_f) ratios are perhaps the most direct indications of relative uplift rate since these are measured at or near the interface of the mountain range and the piedmont where tectonic perturbations, which cause base-level fall, originate from (Bull, 2008). We also measure volume-to-area ratio (R_{VA}) and hypsometric integral (HI), which encompass effects of both hillslope and fluvial processes within the entire drainage basin, rather than just one aspect or section of the tectonic landform. We also measure hypsometric curve statistical moments since these further describe characteristics of a basin that the HI value itself cannot reflect. The elongation ratio (R_e), on the other hand, provides a complementary areal-based measure of the relative proportions of lateral erosion and down-cutting taking place in each basin. Lastly, the normalized channel steepness index (k_{sn}) is sensitive to tectonic perturbations and reflects recent activity which we use for along strike variations in uplift rates of individual faults. Geomorphic indices, such as the ones used in this study, have been extensively used for assessment of relative uplift rates in different tectonic settings worldwide (See Table 1 for examples).

We inspected geologic maps from Servicio Geológico Minero Argentino (SEGEMAR), Bing Maps satellite images, and a combination of hillshade, classified slope, and aspect maps derived from the Advanced Spaceborne Thermal Emission and Reflection Radiometer (ASTER) Global Digital Elevation Model Version 2 (GDEM V2) (https://asterweb.jpl.nasa.gov/gdem.asp) to delineate these fault-bounded mountain range fronts. We chose not to use SRTM30 and AW3D30 digital elevation models due to the presence of frequent voids in mountainous regions. Considering the scale of the study area, the features observed, and the nature of measurements for

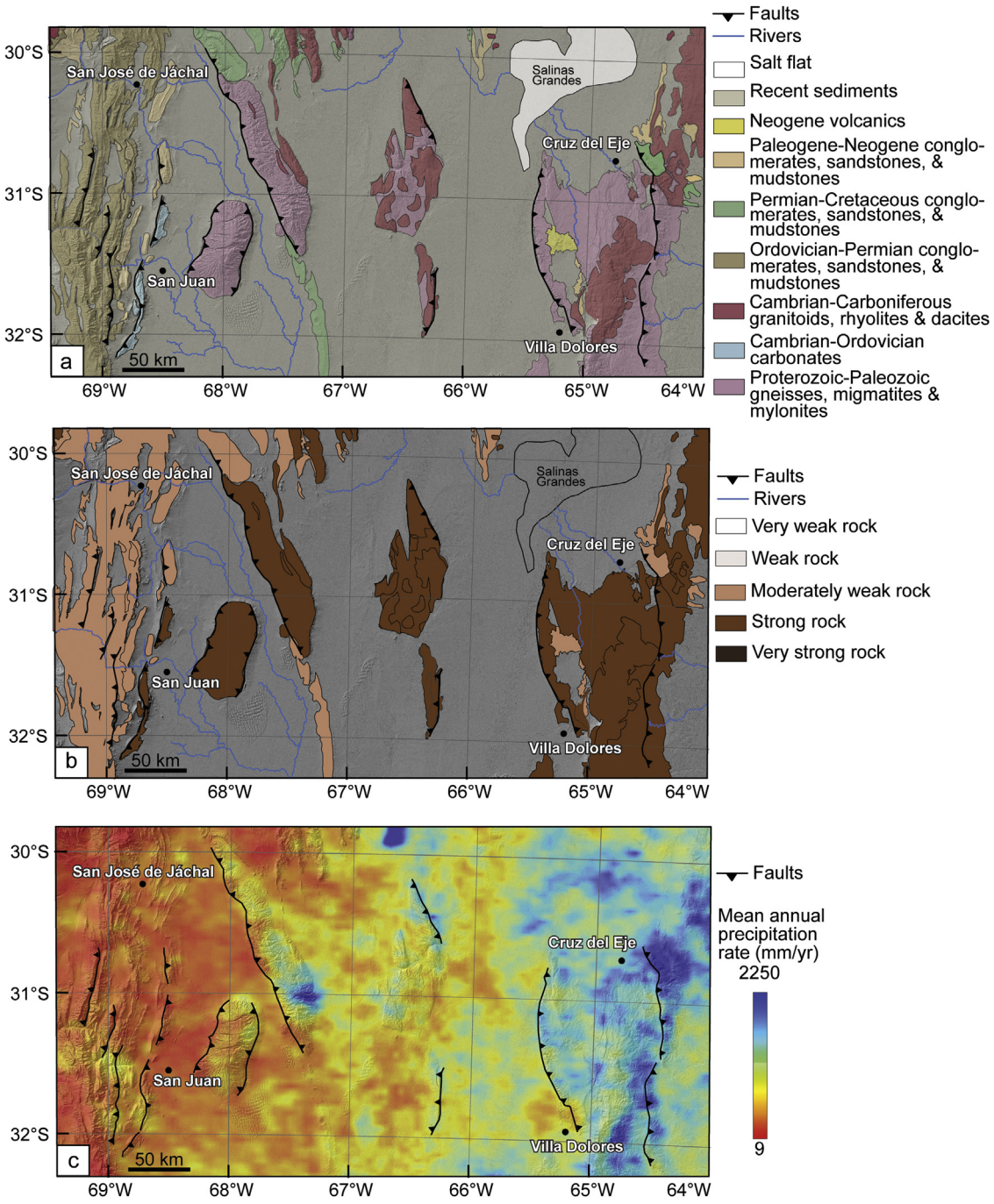

Fig. 4. Geologic, precipitation, and rock erosional resistance maps. a). Generalized geologic map based on 1:250,000 quadrangle maps of SEGEMAR (Instituto de Geología y Recursos Minerales - Intituto de Tecnología Minera (Tecnología Minera; www.segemar.gov.ar/institucional)). b). Rock erosional resistance maps according to Selby (1980). c) Tropical Rainfall Measuring Mission (TRMM) annual average precipitation data from 1998 to 2009.

the particular geomorphic indices we analyze, the vertical and horizontal accuracy of ASTER GDEM V2 are sufficient for measurement aimed at describing regional trends in relative tectonic activity. Existing fault names were used where available; where there were no names for mountain range-bounding faults, we used the name of the range and an indication of which flank it bounds.

For measurement of drainage basin-based geomorphic indices, we delineated basins using the hydrology toolset of ArcGIS. Pourpoints for basin delineation were chosen wherever the range-bounding fault trace intersected a channel flowing from the mountain range. The total number of drainage basins per mountain range front varied from 35 to 203 (Fig. S1. We measured basins with drainage area greater than 250,000 m^2, a minimum threshold value which allowed us to analyze enough basins along strike to have meaningful results, but kept us from analyzing small basins in which non-fluvial processes might dominate, basins that were a product of errors in the DEM (as confirmed on satellite images), or basins that were too youthful to yield reliable measurements for morphometrics (Bull and McFadden, 1977). Additionally, while previous studies have shown that smaller catchments are more sensitive to uplift (Merritts and Vincent, 1989), we demonstrate that there is insignificant correlation between our geomorphic indices measurements and drainage basin area (see Fig. S24–33), except for R_{VA} (see Text S1). This low correlation is due to the small variance in area of drainage basins selected for this study (see data repository-Geomorphic Indices Table).

Table 1
Relative Tectonic Activity Studies Worldwide.

Scale	Regional Tectonic Regime	Number of indices applied	Examples of studies
Single structure	Compressional	1–2	Ahmad et al. (2015)
		> 2	Pedrera et al. (2009), Giaconia et al. (2012)
	Extensional	1–2	–
		> 2	Peters and Van Balen (2007), Özkaymak and Sözbilir (2012), Yıldırım (2014), Özkaymak (2015)
	Strike-slip/Oblique-slip	1–2	–
		> 2	Azor et al. (2002), Gürbüz and Gürer (2008), Selim et al. (2013)
Regional	Compressional	1–2	Silva et al. (2003), Gao et al. (2013)
		> 2	Wells et al. (1988), El Hamdouni et al. (2008), Pérez-Peña et al. (2010), Alipoor et al. (2011), Viveen et al. (2012), Azañón et al. (2012), Arian and Aram (2014), Daxberger and Riller (2015), Ehsani and Arian (2015), Alaei et al. (2017), Gaidzik and Ramírez-Herrera (2017)
	Extensional	1–2	Bull and McFadden (1977)
		> 2	Özsayın (2016)
	Strike-slip/Oblique-slip	1–2	Rockwell et al. (1985), Watkinson and Hall (2017)
		> 2	Chang et al. (2015)

We corroborate our characterization of trends in along-strike relative uplift rates from geomorphic indices with observations from topographic swath profiles (Telbisz et al., 2013) and also use these to make inferences regarding long-term evolution of faults such as fault growth and interactions (e.g., propagation, segment linkage, etc.). In doing this, we assume that topographic swath profiles approximate the cumulative displacement profiles of faults and that initiation of uplift along faults was synchronous.

3.1. Mountain front sinuosity (S_{mf})

S_{mf} is the ratio of the length of the mountain-piedmont junction trace (L_{mf}) to the straight-line length of the mountain front (L_s) (Fig. 5a), which is expressed by the equation:

$$S_{mf} = \frac{L_{mf}}{L_s}$$

Tectonic uplift, through faulting and/or folding, tends to create and maintain a nearly linear mountain front, while erosion and deposition tends to make the trace of the mountain front more irregular. Sinuosity of mountain fronts thus reflects the balance between tectonic uplift and erosion rates. A sinuosity value of 1 corresponds to a perfectly linear mountain front trace, and therefore reflects very high tectonic activity, S_{mf} values close to or less than 1.4 generally indicate high uplift rate (Bull and McFadden, 1977), while an increasingly higher sinuosity value reflects lower tectonic activity (Bull and McFadden, 1977). On average, a kilometer of retreat of the mountain front takes take places after more than 1 my (Bull, 2008).

In ArcGIS, we traced mountain fronts initially by using ASTER GDEM V2-derived maps: a hillshade map layer overlain by a translucent slope layer classified as <10° and >10° to indicate alluvial fans and bedrock mountain front, respectively, and an aspect map layer to check the consistency in the general slope direction of the mountain front trace. We then created the detailed 1:10,000 scale traces by counterchecking our initial crude trace with Bing maps satellite images. S_{mf} was calculated for each major fault segment and minor bends and steps within fault segments.

3.2. Valley floor width to valley height ratio (V_f)

V_f is the ratio of the width of the valley floor to the average height of the valley (Fig. 5b), given by the equation:

$$V_f = \frac{2V_{fw}}{(E_{ld} - E_{sc}) + (E_{rd} - E_{sc})}$$

where V_{fw} is the valley floor width; E_{ld} is the elevation of the left valley divide; E_{rd} is the elevation of the right valley divide; and E_{sc} is the average valley floor elevation. V_f provides a way of distinguishing a valley that is being shaped primarily by active downcutting associated with base level fall from one that is being shaped by lateral erosion of hillslopes. As uplift is associated with river downcutting, a narrower valley floor which corresponds to a lower V_f value, is associated with higher level of tectonic activity (Bull and McFadden, 1977). Because valley floors tend to become progressively narrower upstream and progressively wider downstream, a standard distance from the mountain front (ranging from 0.5 to 1 km) for measuring the V_f is usually assigned (Bull and McFadden, 1977). V_f values also vary depending on basin size, discharge, and rock erodibility. Therefore, basin size, amount of average precipitation, and geology was all taken into account in comparing values in different areas. V_f values from 0.5 to 0.05, are characteristic of narrow, deeply incised, V-shaped channels indicative of very high uplift rates (Bull, 2008), whereas values close to or greater than 1 are characteristic of U-shaped channels indicative of low uplift rates. In arid to semi-arid regions, V_f is effective for describing changes in uplift rate for the past 10–100 ky (Bull, 2008).

We measured V_f over a narrow range of drainage basin area (1-2 km^2) for consistency since smaller streams tend to maintain downcutting much longer compared to larger basins (Bull and McFadden, 1977). We constructed cross-sections from ASTER DEM watershed clip-outs at a distance of 500 m upstream by using the 'interpolate line' and 'profile graph' tool of ArcGIS.

3.3. Basin elongation ratio (R_e)

Drainage basins of tectonically active mountain ranges are typically elongate while drainage basins of less active and inactive mountain ranges tend to be more circular (Canon, 1976; Ramírez-Herrera, 1998). The shape of a drainage basin can therefore be used as an indicator for comparing tectonic activity among ranges. A basin's shape can be described by a ratio of the diameter of a circle of same area as the basin to the drainage basin's length (Fig. 5c), given by the equation (Schumm, 1956):

$$R_e = \frac{D_c}{L_b} = \frac{2}{l}\sqrt{\frac{A}{\pi}}$$

where D_c is the diameter of a circle of same area as the basin; L_b is the basin length; and A is the area of the basin. Shapes defined by the elongation ratio are as follows: circular (0.9–1.0), oval (0.8–0.9), slightly elongated (0.7–0.8), elongated (0.5–0.7), and very elon-

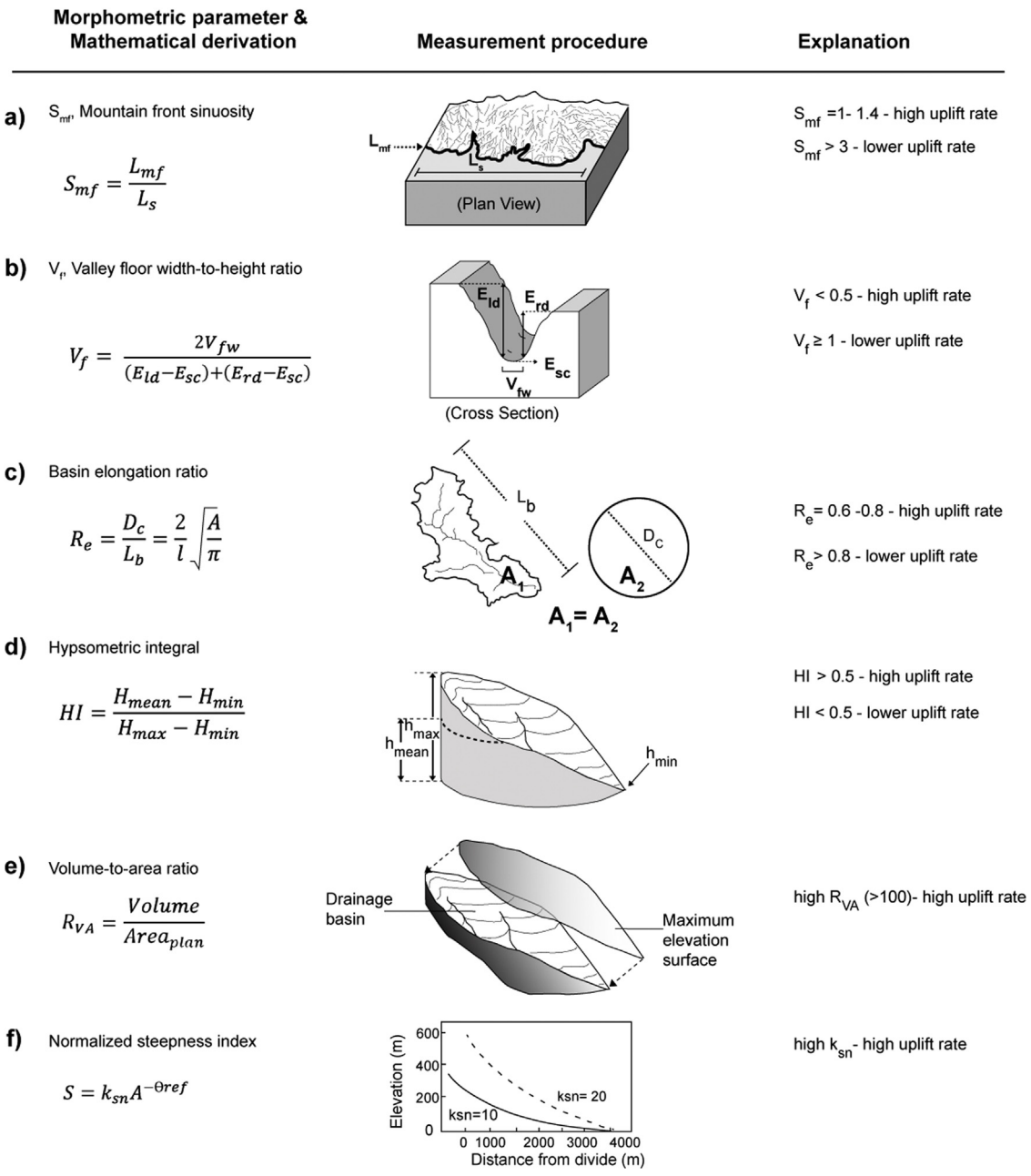

Fig. 5. Geomorphic indices. Diagrams of the different geomorphic indices, the formulas used to compute these, and notes on how these values are interpreted.

gated (< 0.5). According to Strahler (1952), basin elongation ratio varies with climatic type and geology, but typically ranges from 0.6 to 1. Elongated basins, with R_e values of 0.6-0.8, are associated with areas of high-relief and steep slopes which are characteristic of high relative uplift; while circular basins, with R_e values close to 1, are associated with areas of low-relief and gentle slopes which are characteristic of low uplift rate.

We measured the length of each basin from each basin's convex hull, which is delineated using the minimum bounding geometry function of ArcGIS and extracted the area from the attributes table of the drainage basin clipping polygon.

3.4. Hypsometric attributes

A **hypsometric curve** describes the distribution of elevations of landscapes of different scales, including drainage basins (Strahler, 1952). It is a plot of normalized cumulative area (x-axis) against normalized relief (y-axis) of a drainage basin. The area under the hypsometric curve, called the **hypsometric integral (HI)** (Fig. 5d), can be computed to infer the basin maturity. The hypsometric integral (HI) is calculated from three values using the following equation:

$$HI = \frac{H_{mean} - H_{min}}{H_{max} - H_{min}}$$

where h_{mean} is the mean elevation; h_{min} is the minimum elevation; and h_{max} is the maximum elevation. Values range between 0 to 1; a mature basin has a value of around 0.5 (Carson and Kirkby, 1972) or 0.6 (Chorley and Kennedy, 1971). A high hypsometric integral value likely indicates that not as much material from the higher elevation areas have been eroded and therefore suggests a relatively young landscape produced by high uplift rates (Chen et al., 2003; Lifton and Chase, 1992).

The shape of the hypsometric curve can be indicative of topographic maturity of a landscape (Strahler, 1952). In fact, describing the shape of the hypsometric curve may be more useful than a single value, like hypsometric intergral, especially because the hypsometric integral value does not change much in time once it reaches below 0.6 or 0.5, despite potentially corresponding to different forms of hypsometric curves. A measure of the skewness and kurtosis of the hypsometric curve (which is a cumulative distribution function), can be derived from polynomial coefficients of a polynomial function fit through the hypsometric curve. The **skewness (Sk)** describes the amount of headward erosion in the upper reaches of a basin, while **kurtosis (Kur)** describes the amount of erosion on both the upper and lower reaches of a basin. Skewness and kurtosis of the first derivative of the hypsometric curve (a density function), called **density skewness (Dsk)** and **density kurtosis (Dkur)**, indicate the rate of slope change and midbasin slope, respectively (Harlin, 1978). We computed all of these attributes on CalHypso, an ArcGIS add-in tool by Pérez-Peña et al. (2009). Inputs for this tool were the drainage basin polygons and the DEM of the area.

3.5. Volume to area ratio (R_{VA})

Drainage basin volume-to-area ratio, a measure of a basin's mean depth, increases with the rate and amount of fault offset (Schumm and Parker, 1973; Harbor, 1997; Ouchi, 2002; Bonnet and Crave, 2003; Lague et al., 2003). A ratio of the drainage basin volume to its planimetric area ($area_{plan}$) (Fig. 5e), is expressed by the equation:

$$R_{VA} = \frac{Volume}{Area_{plan}}$$

By normalizing the basin volume by drainage area, drainage basins of varying sizes can be directly compared. It has also been used to quantitatively distinguish range-front fault-related base-level fall from a distal base level fall or base-level stability (Frankel and Pazzaglia, 2006). R_{VA} values greater than 100 are usually indicative of high uplift rates, while values much lower than 100 may be, but not necessarily, indicative of low uplift rate. Actively uplifting basins in their 'constructional phase' can be characterized by low R_{VA} ratios (Frankel and Pazzaglia, 2005).

We extracted both the drainage basin volume and area from DEMs according to the procedures in Frankel and Pazzaglia (2006) and Gaidzik and Herrera (2017). Volume was calculated by subtracting the DEM-based drainage basin topography from a maximum elevation envelope (theoretical pre-erosional surface) which was interpolated from elevations on the drainage divide.

3.6. Normalized channel steepness indices (k_{sn})

The primary control of uplift rate on power-law scaling between bedrock river slope and contributing drainage basin area has been well established (Snyder et al., 2000; Kirby et al., 2003; Wobus et al., 2006; Cyr et al., 2010). Channel steepness of DEM-derived longitudinal stream profiles calculated from this relationship, which have been normalized by contributing drainage basin area, have been widely utilized to delineate tectonic boundaries and to map spatial variations of uplift rate (Fig. 5f).

The equation for normalized steepness index, which is ultimately derived from the stream power incision model, applies a reference concavity to account for the influence of the upstream drainage basin area on the channel slope as follows:

$$S = k_{sn} A^{-\Theta ref}$$

where S is channel slope, A is upstream drainage basin area, and θ_{ref} is the reference concavity. A standard value of 0.45, which is thought of as a good approximation for natural concavity of rivers which ranges from 0.4 to 0.6, is used for the reference concavity (Kirby et al., 2003; Kirby and Whipple, 2012; Snyder et al., 2000). While using k_{sn} in the context of mapping relative uplift rate variations, one should be cautious in distinguishing variations in normalized steepness indices due to tectonic activity from variation due to lithologic contrasts (e.g. Cyr et al., 2014; Duvall et al., 2004), precipitation rate (e.g. Bookhagen and Strecker, 2012), and stream capture (Robl et al., 2017).

For mapping normalized steepness indices, the autoksn function of the Stream Profiler ArcGIS add-in by Geomorphtools was used (http://geomorphtools.geology.isu.edu/Tools/StPro/StPro.htm). Flow accumulation files, a required input in Stream Profiler, were created from a DEM that was clipped using a polygon that combines all the drainage basins of the fault-bounded flank of the range. The output channel steepness indices shapefiles from Stream Profiler were then converted to rasters on which swath profiles of maximum, mean, and minimum k_{sn} were constructed. We used k_{sn} swath profiles only for characterizing along-strike variations in relative uplift rates.

4. Results

Faults in the Precordillera are generally characterized by shorter, segmented traces and cumulative displacement profiles with abrupt breaks, whereas while faults in the Sierras Pampeanas are longer and have more continuous displacement profiles. These differences are best characterized by the Morados-Villicum-Zonda-Pedernal Fault (Figs. 3d1–d4 and 6 a&b) in the Precordillera and the Valle Fertil Fault in the Sierras Pampeanas, (Figs. 3g and 7a&b).

While the geomorphic indices values on both Precordillera and Sierras Pampeanas faults display some variability along strike, faults mostly exhibit a unimodal distribution, characterized by a peak which coincides with measures of central tendency of the data (average and median) (Fig. 9a-i). In a few instances, however, we are able to identify convincing along-strike trends based on conspicuous peaks or troughs in values that we recognize in serval different indices. The most common along-strike variation is a change in values towards the tips of each fault/segment (Figs. 6 & 7; and S4–S13). Some geomorphic index values indicate an increase of relative uplift rate towards the tips, as shown, for instance, by lower S_{mf} values and spikes in k_{sn} at the tips of the Valle Fertil Fault (VF; Fig. 7c–e). Most faults, however, indicate relative uplift rates that are higher towards the center and decrease towards the tips of each fault segment and/or the entire fault, as shown, for example, by the Morados-Villicum-Zonda-Pedernal Fault (Fig. 6). The Morados-Villicum-Zonda-Pedernal Fault is an example of a fault showing taper in indices towards the tips of the segments and tips of the entire fault as well. While some geomorphic indices show trends that tend to mimic the displacement profiles (Fig. 6B), this is more common for faults in the Precordillera (Figs. 6 and S4–S7) than in the Sierras Pampeanas (Fig. 7 and S8–S13). We also observed other trends, such as northward or southward increase/decrease in uplift (Figs. S4, S5, S6, and S9). The Sierras de los Llanos & Sierras de las Minas y Ulapes Fault exhibits a bimodal distribution for some indices (labelled fault h in Fig. 9a, f, g, and h).

We excluded outliers and the values at both fault tip and fault linkage zones (points that fall under areas shaded grey in Figs. 6 and 7; Fig. S4–S23), so that the spread of values in the violin plots of morphometric indices along each fault are more likely to be associated with actual variation in relative uplift rates within and/or among its segments. Since along-strike variation is minimal, if at all present, average values of indices for each fault are likely representative of the faults' overall activity level and yield

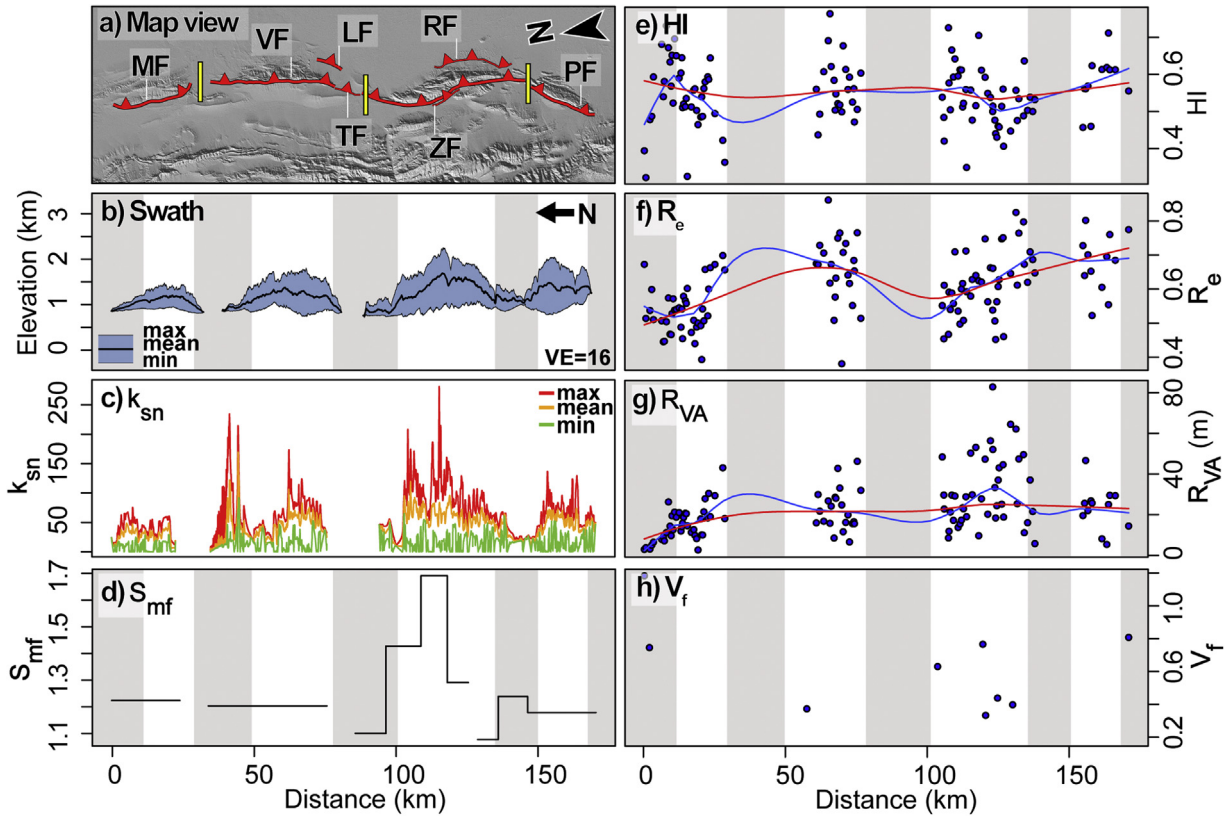

Fig. 6. Morados-Villicum-Zonda-Pedernal Fault. a) Map View. MF—Morados Fault. VF—Villicum Fault. TF—Las Tapias Fault. ZF—Zonda Fault. RF—La Rinconada Fault. PF—Pedernal Fault. LF—La Laja Fault. Yellow bars indicate fault segment boundaries. b) Swath topographic profile. c) K_{sn}. d) S_{mf}. e) HI. f) R_e. g) R_{VA}. h) V_f. The red line and blue lines in graph e, f, and g represent locally weighted regressions with spans of 0.25 and 0.5, respectively. The regions shaded gray are fault tip and fault linkage zones. See Supplementary Fig. S7 for locations of related Quaternary-active scarps, Fig. S12 for statistical moments of the hypsometric curves for basins inspected in e, and Text S5 for more detailed descriptions.

meaningful results for assessing possible regional west-east trends, which is the main objective of this study.

We classified average values of each geomorphic index as reflecting low, moderate, or high relative uplift rate (see Fig. 8). Of all 10 faults, only the Valle Fertil Fault (Fig. 7 and 8) yielded a uniform relative uplift rate classification among all indices (i.e., consistently moderate uplift rates). For all of the other faults, different indices yield ranges of relative uplift rate levels, including some apparent disagreement (instances in which different indices suggest high and low uplift rate for the same fault; Fig. 8). The relative uplift rates inferred from R_{VA}, which are mostly trendless, seem to cause the inconsistency with relative uplift rates inferred from other indices (Figs. 6g, 7 g, and S4g–S13g). These exceptions, as discussed in Section 5, can reflect differences in response times and local conditions, or the sensitivity of different indices to landform maturity.

The values of the different geomorphic indices measured along each of the 10 N-S trending mountain range bounding faults are summarized as violin plots to analyze possible W-E trends and at the same time to display the mean value vis-à-vis the distribution of data from a single fault. Overall, there is little W-E variation in the average values for the different geomorphic indices. Yet, amidst this minimal variation, we observed four subtle features (Fig. 9a–i). The first feature is the close mean geomorphic indices values (except for S_{mf}) for faults west of and including the Morados-Villicum-Zonda-Pedernal Faults in the Precordillera (faults a to d in Figs. 3,8, and 9). The second feature is a step between the Eastern Pie de Palo Fault and Valle Fertil Fault (between faults f and g in Figs. 3,8, and 9), except for R_{VA}, indicating a decrease in relative uplift rate. The third feature is another step between the Valle Fertil Fault and the Sierras de los Llanos and Sierras de las Minas y Ulapes Fault (between faults g and h in Figs. 3,8, and 9), indicating an increase in relative uplift rates. Lastly, there is a local west-to-east decrease in relative uplift rates from Sierras de los Llanos and Sierras de las Minas y Ulapes Fault to Pocho Fault (faults h to j in Figs. 3,8, and 9), except for V_f, likely due to lack of data.

5. Discussion

The observed variability of some geomorphic indices at the tips of and between adjacent segments of faults (linkage zones) in the Precordillera (Figs. 6 and S4–S7) is consistent with their highly segmented morphology (Ellis and Barnes, 2015) and may indicate that these fault segments are still growing and interacting (Densmore et al., 2007). On the other hand, the uniform relative uplift along faults in the Sierras Pampeanas (Figs. 7 and S8–S13), which are characterized by longer traces and more continuous displacements profiles, may suggest that Pampean faults tend to be already hard linked. This difference in segmentation patterns can be attributed to the difference in the geology between these two regions. While reverse/thrust faults are typically highly discontinuous (Aydin, 1988), the hard linkage of faults in the Sierras Pampeanas is probably a consequence of tectonic inheritance (Mora et al., 2009). The observed bimodal distribution for indices for the Sierras de los Llanos & Sierras de las Minas y Ulapes Fault (labelled fault h in Fig. 9a, f, g, and h) is due to an actual significant difference in average geomorphic indices values for these two faults, with most indices pointing to the Sierras de las Minas y Ulapes Fault as having higher relative uplift rate and being more youthful (Fig. S11 and Text S9). While a detailed investigation of the

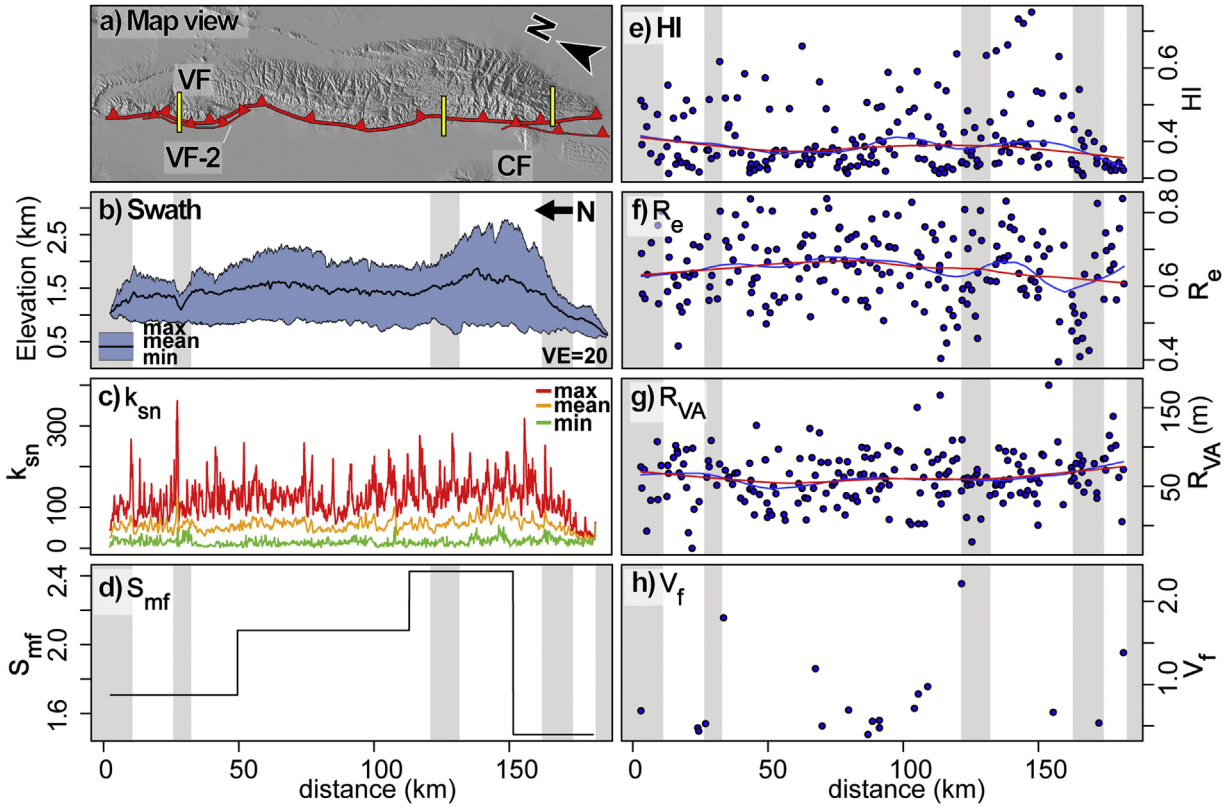

Fig. 7. Valle Fertil Fault. a) Map View. VF— Valle Fertil Fault. VF-2— Valle Fertil Fault Quaternary-active scarps. CF— Las Chacras Fault. Yellow bar/s indicates fault segment boundaries. b) Swath topographic profile. c) K_{sn}. d) S_{mf}. e) HI. f) R_e. g) R_{VA}. h) V_f. The red line and blue lines in graph e, f, and g represent locally weighted regressions with spans of 0.25 and 0.5, respectively. The regions shaded gray are fault tip and fault linkage zones. See Supplementary Fig. S10 for locations of related Quaternary-active scarps, Fig. S15 for statistical moments of the hypsometric curves for basins inspected in e, and Text S8 for more detailed descriptions.

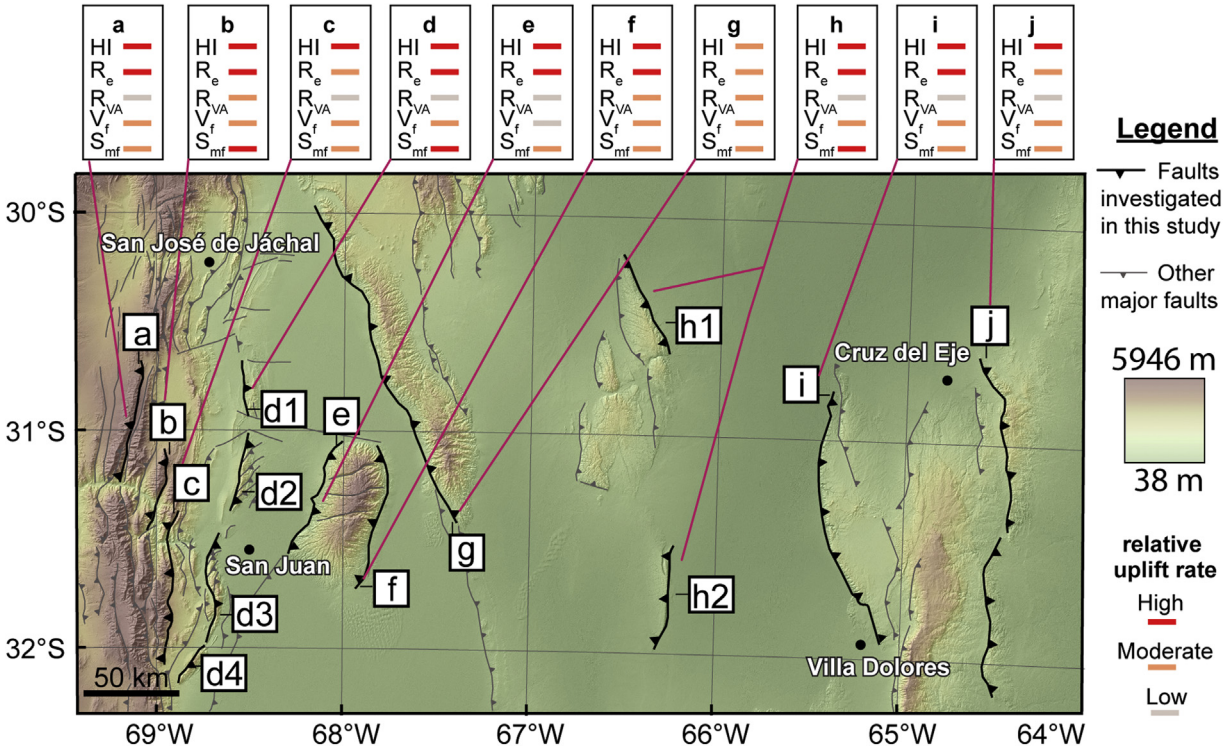

Fig. 8. Summary of relative uplift rates from various geomorphic indices. a—Eastern Sierra del Tigre Fault. b— Eastern Sierra de Cantera Fault. c—Sierra de Osamentas Fault. d (d1-d4)— Morados-Villicum-Zonda-Pedernal Faults. e— Western Pie de Palo Fault. f— Eastern Pie de Palo Fault. g— Valle Fertil Fault. h (h1-h2)— Sierras de los Llanos and Sierras de las Minas y Ulapes Fault. i— Pocho Fault. j— Sierra Chica Fault Zone. See Table S1 for averages of each geomorphic indices.

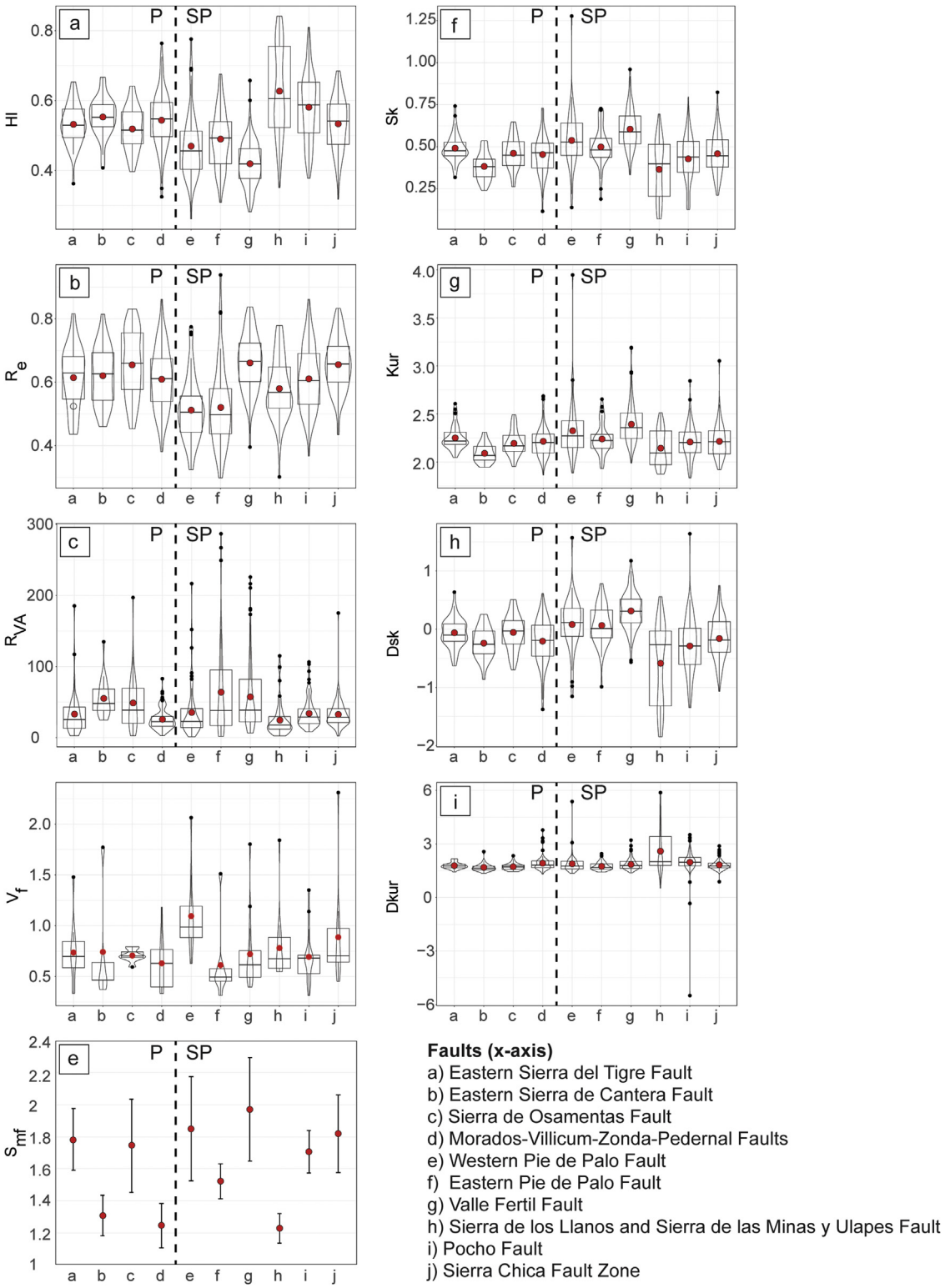

Fig. 9. Graphs of east-west variation in fault-averaged geomorphic indices values. Values from each fault are presented as violin plots (box plots superimposed on density plots) except for 9e. Red dot is the mean value, the top and bottom of the box are the second and third quartiles, respectively, and the black dots are outliers. The vertical broken line is the division between the Precordillera and Sierras Pampeanas regions. For 9e, values are presented as mean and error bars (2 sigma). a) Hypsometric Integral (HI), b) Elongation (R_e), c) Volume-to-area ratio (R_{VA}), d) Valley-floor-width-to-height (V_f) ratio, e) Mountain front Sinuosity (S_{mf}), f) Skewness (Sk), g) Kurtosis (Kur), h) Density Skewness (Dsk), i) Density Kurtosis (Dkur).

behavior and long-term evolution of each individual fault is beyond the scope of our study, these observations demonstrate that analysis of along-strike variation in relative uplift rates can be used for more detailed future investigations of fault growth/linkage. More detailed descriptions of along-strike variations in relative uplift rates and initial interpretations regarding the long-term evolution history of all ten faults are included in the supporting information (Fig. S4–S13 and Text S2-S11).

We use individual relative uplift rate classes for each fault to provide context for any 'inconsisent' relative uplift rates from particular indices to come up with a unified uplift rate classification for each fault. Inconsistencies or exceptions in relative uplift rate classification of faults is introduced mostly by R_{VA} (Fig. 8a, c, d, h, i, and j), and in some cases by R_e. Low R_{VA} values most likely reflect the youth of the drainage basins, since the high relative uplift rates inferred from other geomorphic indices, especially HI (along with Sk, Kur, Dsk, and Dkur), rule out low uplift rate along any of these faults. On the other hand, low R_e values measured where most other indices indicate low relative uplift rate (Fig. S8, Text S6) are usually related either to development of streams on prominent fractures that cross some ranges or to significant stream capture of channels from the opposite flank of the mountain range (Fig. S6, Text S4). We categorize the Eastern Sierra de la Cantera, Morados-Villicum-Zonda-Pedernal, and the Sierras de los Llanos & Sierras de las Minas y Ulapes Faults as having overall high relative uplift rate, the Eastern Sierra del Tigre, Sierra de Osamentas, Eastern Pie de Palo, Valle Fertil, Pocho, Sierra Chica Fault Zone as having overall moderate-to-high relative uplift rate, and the Western Pie de Palo Fault as having low-to-moderate relative uplift rate. Of the faults described as exhibiting moderate to high relative uplift rate, the Eastern Sierra del Tigre, Eastern Sierra de la Cantera, and Sierras de los Llanos & Sierras de las Minas y Ulapes, Pocho faults could benefit the most from more detailed assessment of activity as the hazards associated with these faults are relatively unknown.

We interpret variations in average geomorphic indices values among faults in a W-E transect in terms of uplift rates, taking into consideration both W-E gradients in rock erosional resistance and annual average precipitation rate (Fig. 4b and c). While numerous studies have shown how lithological variation can complicate interpretation of trends in geomorphic indices in terms of rates of uplift (Bull, 2008; Keen-Zebert et al., 2017; van Laningham et al., 2006; Walcott and Summerfield, 2008), the uniform relative uplift rates from west to east renders a lithological influence unlikely. We only define two rock strength distributions, with slightly more resistant rocks in the Sierras Pampeanas compared to the Precordillera (Bonalumi et al., 1999; Candiani et al., 2001, 2010; Cardó and Díaz, 2005; Costa et al., 2001a; Costa et al., 2001b; Fauqué et al., 2004; Furque et al., 1998; Miró et al., 2005; Ragona et al., 1995; Ramos and Vujovich, 2000; Ramos, Caminos, et al., 2000; Ramos et al., 2010; Vujovich et al., 1998). We did not observe a change in morphometric indicators corresponding to the change in lithology. In fact, if actual levels of relative uplift rates on faults in the east are obscured due to the slightly resistant lithology of the Sierras Pampeanas, this will result in enhancement of the eastward decrease in relative shortening rates. Climate is fairly uniform up to the eastern front of the Valle Fertil Fault, where there is a noticeable increase in average precipitation rate. We assess the potential role of precipitation in the discussion of subtle relative uplift rate trends observed in the Sierras Pampeanas.

Overall, the average values of geomorphic indices among the 10 faults vary minimally (Fig 9a–i) and are less significant than might be expected given the geologic and geodetic data which point towards strongly varying distribution of shortening deformation across the region. This apparent discrepancy can be reconciled by considering fault dip. When the general difference between shallower dipping faults in the thin-skinned Precordillera to the west and more steeply dipping faults in the thick-skinned Sierras Pampeanas to the east is considered (Ramos et al., 2002; Richardson et al., 2013; Siame et al., 2015), the observed relative uplift rates on these 10 faults translate to generally higher relative shortening rates for the Precordillera fold-and-thrusts (in the west) than the Sierra Pampean thick-skinned reverse faults (in the east). Agreement between this finding, GPS gradients and relative tectonic activity from geomorphic indices could indicate that there has been no stress significant field change since at least the Pleistocene. However, additional quantitative slip rate studies over wider time intervals in the late Quaternary are necessary to test this scenario.

The local trends inferred from the fault-averaged morphometrics, such as the uniform uplift rates in the Precordillera, steps in relative uplift rates between several Western Sierras Pampeanas faults, and local west-to-east decreasing uplift rates the eastern Sierras Pampeanas show associations with structural style and the tectonic evolution these structures. Within the Precordillera, geomorphic index values are relatively uniform, with the exception of S_{mf}. These uniform values may be explained by an even distribution of strain throughout this fold-and-thrust belt, a trend which is consistent both with GPS gradients (Brooks et al., 2003) and currently available geomorphic-derived slip rates (Costa et al., 2015a, 2015b; Costa et al., 2018; Rimando et al., 2019; Rockwell et al., 2014; Salomon et al., 2013; Schmidt et al., 2011; Schoenbohm et al., 2013; and Siame et al., 2002, 2006).

Morphometric indices change significantly between the Eastern Pie de Palo and the Valle Fertil (faults f and g in Figs. 3 and 9), a trend which is consistent with other data. The Eastern Pie de Palo in particular has been well studied and characterized through geologic, geomorphic, seismic, and thermochronologic studies as a highly active (if not the most active) structure in the region (Bellahsen et al., 2016; Ramos et al., 2002; Siame et al., 2015). Although the 0.5 ± 0.1 mm/yr to 0.8 ± 0.4 mm/yr slip rates estimated on the EPF (Siame et al., 2015) may not comprise a significant portion of the total shortening rate of the Andean Orogenic Front on different timescales (Ramos et al., 2002, 2004; Zapata and Allmendinger, 1996; Kendrick et al., 1999, 2001, 2003, 2006; Brooks et al., 2003), it has been the locus of the country's strongest earthquakes, concentrating most of the region's seismic moment release. This seems to be consistent with average values of Re, R_{VA}, and V_f, all suggesting exceptionally high relative uplift rates on this fault, significantly higher than that for the Valle Fertil and Sierras de los Llanos and Sierras de Las Minas y Ulapes Faults to the east. A similar increase in uplift rates is recorded by morphometric data between the Valle Fertil Fault and the Sierras de los Llanos and Sierras de Las Minas y Ulapes Faults (faults g and h in Figs. 3 and 9), but this cannot be independently corroborated as quantitative Quaternary uplift rates have not been determined.

The westward local increase in relative uplift rates in the Sierras Pampeanas, indicated by most indices from the Sierra Chica Fault Zone to the Sierras de los Llanos and Sierras de las Minas y Ulapes Fault (faults h, i, and j in Figs. 9a–i), may reflect westward migration of deformation in the Sierras Pampeanas between ~6–5.5 Ma and ~3 Ma (Jordan et al., 1983a, 1983b; Ramos et al., 2002). Activity on the eastern Sierras Pampeanas structures may have begun to wane as the wave of deformation started migrating to the west. This interpretation is consistent with the westward increase in decadal-scale GPS slip rates (Brooks et al., 2003). Alternatively, the westward decrease in precipitation could also cause this gradient in geomorphic indices, although the relatively high HI values on these faults suggest that the effect of precipitation is low.

While the subduction of the nearly-horizontal Pampean flat slab caused permanent shortening features to reach as far as ~700 km east of the plate boundary, it appears that shortening rates on these structures progressively decrease towards the east beginning at the Sierras de los Llanos and Sierras de Las Minas y Ulapes Faults (fault h in Figs. 3 and 9). This onset of lower relative uplift rates coincides spatially in the subsurface with the resumption of a steeper angle of the subduction. In addition, although the Eastern Pie de Palo Fault is consistently shown as having a comparatively high relative uplift rate, several other faults also exhibit high activity, belonging to both thick- and thin-skinned systems within the Pampean flat slab region.

6. Conclusions

Geomorphic indices show the spatial distribution of relative uplift rates for ten faults along a W-E transect in the back-arc region of the seismically active Pampean flatslab segment of Argentina. Variation in values of geomorphic indices along a fault are interpreted as along-strike variation in uplift rates and/ or segmentation. Along individual faults, relative uplift rates are usually higher at the center of each fault and locally at the center of each segment of a fault and decrease towards the fault terminations. Decrease in measured relative uplift rate towards fault tips is interpreted as being the result of longer response times of fault-tip catchments to fault growth-related increase in uplift rates, rather than lower uplift rates. Swath profiles, which reflect cumulative displacement of a fault, show a consistent spatial correspondence between areas of higher cumulative displacement (centers of faults) and higher inferred relative uplift rate. In calculating averages of geomorphic indices per fault, we therefore excluded values near the fault tips. We interpret the Eastern Sierra de la Cantera, Morados-Villicum-Zonda-Pedernal, and Sierras de los Llanos & Sierras de las Minas y Ulapes Faults as having overall high relative uplift rate from averaged values of geomorphic indices. The Eastern Sierra del Tigre, Sierra de Osamentas, Eastern Pie de Palo, Valle Fertil, Pocho, and Sierra Chica Faults have overall moderate to high relative uplift rates. Only the Western Pie de Palo Fault shows evidence for overall low-to-moderate relative uplift rates.

While there is no major regional W-E trend in inferred relative uplift rates, our data highlight subtle trends and characteristics that appear to be related to the structural style and the tectonic evolution the structures:

1) The thin-skinned Precordillera faults in the west display nearly uniform mean geomorphic index values, which is consistent with interpretations of even distribution of strain throughout the numerous structures of the Precordillera fold-and-thrust belt based on GPS gradients and geomorphic-derived slip rates. Relative shortening rates are higher in the Precordillera than the Sierras Pampeanas, when fault dip differences between these regions are considered. This similarity in trend with GPS gradients may indicate that there has been no stress field change since at least the Pleistocene. However, further slip rate studies over broader time intervals in the late Quaternary are necessary to support this.
2) The match in the westward trend of younger deformation in the thick-skinned Sierras Pampeanas region and the local westward increase in uplift rates inferred from geomorphic indices may indicate waning of activity on older faults as deformation migrated westward over the last few millions years. It is possible, however, that the region may have had a more complex spatiotemporal strain distribution on shorter timescales (10^1–10^5 years).
3) Noticeably higher relative uplift rate on the Eastern Pie de Palo Fault compared to other structures in the Sierras Pampeanas is consistent with previous studies that appraise the Eastern Pie de Palo Fault as a highly active (if not the most active) structure in the region.

In summary, while flat-slab subduction has resulted in an exceptionally wide deformation zone that extends 700 km east of the Peru-Chile Trench, it proceeds so with a gradual eastward decrease of relative shortening rates (at least into Pleistocene), with only a few sites of exceptionally high activity in between. This decrease becomes pronounced at the Sierras de los Llanos and Sierras de Las Minas y Ulapes Faults, which coincides with the same longitudinal range as the slab's resumption of a steeper angle of subduction. In addition, deformation is not entirely localized. Although the Eastern Pie de Palo Fault shows comparatively high relative uplift rate, there are several other thick- and thin-skinned thrust/reverse faults also with high activity, found throughout the Pampean flat slab region.

When using geomorphic indices to assess relative uplift rate variations along a fault or among several faults, we show that it is better to interpret these indices collectively rather than individually, as geomorphic indices may vary in sensitivity/response times and degree to which these can be indicative of tectonics vs. landform maturity (e.g., use of HI in conjunction with Sk, Kur, Dsk, and Dkur). Finally, areas indicated in this study as having relatively higher uplift rates, can be used as basis to identify priority sites for more detailed studies for determining activity and seismogenic capability. To date, of the faults that have been characterized as having moderate to high relative uplift rate, the Eastern Sierra del Tigre, Eastern Sierra de la Cantera, and Sierras de los Llanos & Sierras de las Minas y Ulapes, Pocho faults have not yet been as well studied. Therefore, these faults present a potential for future measurement of quantitative slip-rates and assessment of seismic hazards.

Declaration of Competing Interest

The authors declare that they have no known competing financial interests or personal relationships that could have appeared to influence the work reported in this paper.

Acknowledgments

The authors would like to thank Prof. Pierre-Yves Robin and Prof. Rebecca Ghent for the valuable discussions. Special thanks to Mitchell McMillan for his assistance with using R for making graphs. The authors are also grateful to the three anonymous reviewers, and Editors Martin Stokes and Simon Allen for handling this manuscript. This research was funded by a Natural Sciences and Engineering Research Council (NSERC) of Canada Discovery grant to Lindsay Schoenbohm (University of Toronto).

Appendix A. Supplementary data

Supplementary material related to this article can be found, in the online version, at doi:https://doi.org/10.1016/j.geomorph.2019.106908.

References

Abraham de Vázquez, E., Garleff, K., Liebricht, H., Regairaz, A., Schabitz, F., Squeo, F., Sting, H., Veit, H., Villagrán, C., 2000. Geomorphology and paleoecology of the arid diagonal in southern South America. Zeitschrift für angewandte Geologie, 55–61.

Ahmad, S., Alam, A., Ahmad, B., Bhat, M.I., Bhat, M.S., 2015. Geomorphic evidence of unrecognized Balapur fault segment in the southwest Kashmir basin of northwest Himalayas. Geomorphology 250, 159–172.

Alaei, M., Dehbozorgi, M., Ghassemi, M.R., Nozaem, R., 2017. Evaluation of relative tectonic activity of Buin Zahra-Avaj area, northern Iran. Arab. J. Geosci. 10 (10), 229.

Alipoor, R., Poorkermani, M., Zare, M., El Hamdouni, R., 2011. Active tectonic assessment around Rudbar Lorestan dam site, High Zagros Belt (SW of Iran). Geomorphology 128 (1), 1–14.

Allmendinger, R.W., Jordan, T.E., Kay, S.M., Isacks, B.L., 1997. The evolution of the Altiplano-Puna plateau of the Central Andes. Annu. Rev. Earth Planet. Sci 25 (1), 139–174.

Amidon, W.H., Fisher, G.B., Burbank, D.W., Ciccioli, P.L., Alonso, R.N., Gorin, A.L., et al., 2017. Mio-Pliocene aridity in the south-central Andes associated with Southern Hemisphere cold periods. Proc. Natl. Acad. Sci. 114 (25), 6474–6479.

Anderson, M., Alvarado, P., Zandt, G., Beck, S., 2007. Geometry and brittle deformation of the subducting Nazca Plate, Central Chile and Argentina. Geophys. J. Int. 171 (1), 419–434.

Arian, M., Aram, Z., 2014. Relative tectonic activity classification in the Kermanshah area, western Iran. Solid Earth 5 (2), 1277.

Attal, M., Cowie, P.A., Whittaker, A.C., Hobley, D., Tucker, G.E., Roberts, G.P., 2011. Testing fluvial erosion models using the transient response of bedrock rivers to tectonic forcing in the Apennines, Italy. J. Geophys. Res. Earth Surf. 116 (F2).

Aydin, A., 1988. Discontinuities along thrust faults and the cleavage duplexes. Geol. Soc. Am., Special Paper 222, 223–232.

Azañón, J.M., Pérez-Peña, J.V., Giaconia, F., Booth-Rea, G., Martínez-Martínez, J.M., Rodríguez-Peces, M.J., 2012. Active tectonics in the central and eastern Betic Cordillera through morphotectonic analysis: the case of Sierra Nevada and Sierra Alhamilla/Tectónica activa en la Cordillera Bética Oriental y Central mediante análisis morfotectónico: el caso de Sierra Nevada y Sierra Alhamilla. J. Iber. Geol. 38 (1), 225.

Azor, A., Keller, E.A., Yeats, R.S., 2002. Geomorphic indicators of active fold growth: South Mountain–Oak Ridge anticline, Ventura basin, southern California. Geol. Soc. Am. Bull. 114 (6), 745–753.

Bastias, H., 1985. Fallamiento Cuaternario en la region sismotectonica de precordillera: San Juan, Argentina, Facultad de Ciencias Exactas, Físicas y Naturales. Universidad Nacional de San Juan, pp. 160, Doctoral dissertation, Tesis Doctoral inedita.

Bellahsen, N., Sébrier, M., Siame, L., 2016. Crustal shortening at the Sierra Pie de Palo (Sierras Pampeanas, Argentina): near-surface basement folding and thrusting. Geol. Mag. 153 (5–6), 992–1012.

Bonalumi, A., Martino, R., Baldo, E., Zarco, J., Sfragulla, J., Carignano, C., Kraemer, P., Escayola, M., Tauber, A., Cabanillas, A., Juri, E., Torres, B., 1999. Memoria Hoja geológica 3166-IV, Villa Dolores. Servicio Geológico Minero Argentino, Buenos Aires.

Bonnet, S., Crave, A., 2003. Landscape response to climate change: insights from experimental modeling and implications for tectonic versus climatic uplift of topography. Geology 31 (2), 123–126.

Bookhagen, B., Strecker, M.R., 2012. Spatiotemporal trends in erosion rates across a pronounced rainfall gradient: examples from the southern Central Andes. Earth Planet. Sci. Lett. 327, 97–110.

Brooks, B., Bevis, M., Smalley, R., Kendrick, E., Manceda, R., Lauría, E., et al., 2003. Crustal motion in the Southern Andes (26°–36°S): Do the Andes behave like a microplate? Geochem. Geophys. Geosystems 4 (10), 1–14.

Bruniard, E.D., 1982. La diagonal árida Argentina: un límite climático real. Revista Geográfica 95, 5–20.

Bull, W.B., 2008. Tectonic Geomorphology of Mountains: a New Approach to Paleoseismology. John Wiley & Sons.

Bull, W.B., McFadden, L.D., 1977. Tectonic geomorphology North and South of the Garlock Fault, California. In: Doehring, D.O. (Ed.), Geomorphology in Arid Regions: A Proceedings Volume of the 8th Annual Geomorphology Symposium. State University of New York, Binghamton, 23-24 September 1977, pp. 115–138.

Burbank, D.W., Anderson, R.S., 2001. Tectonic Geomorphology. John Wiley & Sons.

Burbank, D.W., Anderson, R.S., 2012. Tectonic Geomorphology, 2nd edition. Wiley, pp. 454.

Cahill, T., Isacks, B., 1992. Seismicity and shape of the subducted Nazca Plate. J. Geophys. Res. 97 (B12), 17503–17529.

Candiani, J., Carignano, C., Stuart-Smith, P., Lyons, P., Miró, R., López, H., 2001. Memoria Hoja geológica 3166-II, Cruz del Eje. Servicio Geológico Minero Argentino, Buenos Aires.

Candiani, J.C., Gaido, M.F., Miró, R.C., Carignano, C.A., 2010. Hoja Geológica 3163-I Jesús María. Servicio Geológico Minero Argentino, Buenos Aires.

Canelo, H.N., Nóbile, J.C., Dávila, F.M., 2019. Uplift analysis on a pericratonic region: An example in the Sierras de Córdoba (29°–34° S), Argentina. Geomorphology 329, 81–98.

Canon, P.J., 1976. Generation of explicit parameters for a quantitative geomorphic study of the Mill Creek drainage basin. Oklahoma Geol. Notes 36 (1), 3–16.

Cardó, R., Díaz, I.N., 2005. Memoria Hoja Geológica 3169-I. Rodeo. Servicio Geológico Minero Argentino, Buenos Aires.

Caselli, A., Net, L., Litvak, V., Limarino, C., Poma, S., Gutierrez, P., 1999. Memoria Hoja Geológica 3166-I. Chamical. Servicio Geológico Minero Argentino, Buenos Aires.

Chang, Z., Sun, W., Wang, J., 2015. Assessment of the relative tectonic activity in the Bailongjiang Basin: insights from DEM-derived geomorphic indices. Environ. Earth Sci. 74 (6), 5143–5153.

Chen, Y.C., Sung, Q., Cheng, K.Y., 2003. Along-strike variations of morphotectonic features in the Western Foothills of Taiwan: tectonic implications based on stream-gradient and hypsometric analysis. Geomorphology 56 (1-2), 109–137.

Chorley, R.J., Kennedy, B.A., 1971. Physical Geography: a Systems Approach. Prentice-Hall International. Inc., London.

Clayton, K., Shamoon, N., 1998. A new approach to the relief of Great Britain: II. A classification of rocks based on relative resistance to denudation. Geomorphology 25 (3–4), 155–171.

Cortés, J.M., Vinciguerra, P., Yamín, M., Pasini, M.M., 1999. Tectónica cuaternaria de la Región Andina del Nuevo Cuyo (28° -38° LS). En Geología Argentina. Servicio Geológico Minero Argentino, Subsecretaría de Minería, Buenos Aires.

Costa, C., 1999. Tectónica Cuaternaria en las Sierras Pampeanas. In: Caminos, R. (Ed.), Geología Argentina, 29. SEGEMAR, Anales, pp. 779–784.

Costa, C., Machette, M.N., Dart, R., Bastías, H., Paredes, J.D., Perucca, L.P., Tello, G.E., Haller, K.M., 2000. Map and Database of Quaternary Faults and Folds in Argentina. Us Geological Survey Open-File Report, 108., pp. 75.

Costa, C.H., Murillo, M.V., Sagripanti, G.L., Gardini, C.E., 2001a. Quaternary intraplate deformation in the southeastern Sierras Pampeanas, Argentina. J. Seismol. 5 (3), 399–409.

Costa, C.H., Gardini, C.E., Ortíz Suárez, A.E., Chiesa, J.O., Ojeda, G.E., Rivarola, D.L., et al., 2001b. Hoja Geológica 3366-I San Francisco del Monte de Oro. Servicio Geológico Minero Argentino, Buenos Aires.

Costa, C.H., Gardini, C.E., Chiesa, J.O., Ortíz Suárez, A.E., Ojeda, G.E., Rivarola, D.L., et al., 2001c. Hoja Geológica 3366-III San Luis. Servicio Geológico Minero Argentino, Buenos Aires.

Costa, C.H., Audemard, M., Bezerra, F.H.R., Lavenu, A., Machette, M.N., Paris, G., 2006. An overview of the main Quaternary deformation of South America. Revista de la Asociación Geológica Argentina 61 (4), 461–479.

Costa, C., Massabie, A., Sagripanti, G., Brunetto, E., Coppolecchia, M., 2014. Neotectónica de la provincia de Córdoba. In: Geología y Recursos Naturales de la Provincia de Córdoba, Relatorio del XIX Congreso Geológico Argentino., pp. 725–748.

Costa, C.H., Owen, L.A., Ricci, W.R., Johnson, W.J., Halperin, A.D., 2018. Holocene activity and seismogenic capability of intraplate thrusts: insights from the Pampean ranges, Argentina. Tectonophysics 737, 57–70.

Costa, C.H., Ahumada, E.A., Vázquez, F.R., Kröhling, D.M., 2015a. Holocene shortening rates of an Andean-front thrust, Southern Precordillera, Argentina. Tectonophysics 664, 191–201.

Costa, C.H., Ahumada, E.A., Gardini, C.E., Vázquez, F.R., Diederix, H., 2015b. Quaternary Shortening at the Orogenic Front of the Central Andes of Argentina: the Las Peñas Thrust System. Geological Society, London, pp. 245–266, Special Publications, 399(1).

Cyr, A.J., Granger, D.E., Olivetti, V., Molin, P., 2010. Quantifying rock uplift rates using channel steepness and cosmogenic nuclide–determined erosion rates: examples from northern and southern Italy. Lithosphere 2 (3), 188–198.

Cyr, A.J., Granger, D.E., Olivetti, V., Molin, P., 2014. Distinguishing between tectonic and lithologic controls on bedrock channel longitudinal profiles using cosmogenic 10Be erosion rates and channel steepness index. Geomorphology 209, 27–38.

Daxberger, H., Riller, U., 2015. Analysis of geomorphic indices in the southern Central Andes (23–28 S): evidence for pervasive Quaternary to Recent deformation in the Puna Plateau. Geomorphology 248, 57–76.

Densmore, A.L., Gupta, S., Allen, P.A., Dawers, N.H., 2007. Transient landscapes at fault tips. J. Geophys. Res. Earth Surf. 112 (F3).

Duvall, A., Kirby, E., Burbank, D., 2004. Tectonic and lithologic controls on bedrock channel profiles and processes in coastal California. J. Geophys. Res. Earth Surf. 109 (F3).

Ehsani, J., Arian, M., 2015. Quantitative analysis of relative tectonic activity in the Jarahi-Hendijan basin area, Zagros, Iran. Geosci. J. 19 (4), 751–765.

El Hamdouni, R., Irigaray, C., Fernández, T., Chacón, J., Keller, E.A., 2008. Assessment of relative active tectonics, southwest border of the Sierra Nevada (southern Spain). Geomorphology 96 (1), 150–173.

Ellis, M.A., Barnes, J.B., 2015. A global perspective on the topographic response to fault growth. Geosphere 11 (4), 1008–1023.

Engdahl, E.R., Villaseñor, 2002. Global seismicity: 1900-1999. In: International handbook of earthquake and engineering seismology., pp. 665–690.

Engdahl, E.R., van der Hilst, R., Buland, R., 1998. Global teleseismic earthquake relocation with improved travel times and procedures for depth determination. Bull. Seismol. Soc. Am. 88 (3), 722–743.

Fauqué, L.E., Limarino, C.O., Vujovich, G.I., Fernández Dávila, L., Cegarra, M.I., Escosteguy, L.D., 2004. Hoja Geológica 2969-IV Villa Unión, Provincias de La Rioja y San Juan. Servicio Geológico Minero Argentino, Buenos Aires.

Fielding, E.J., Jordan, T.E., 1988. Active deformation at the boundary between the Precordillera and Sierras Pampeanas, Argentina, and comparison with ancient Rocky Mountain deformation. Geol. Soc. Am. Mem. 171, 143–164.

Frankel, K.L., Pazzaglia, F.J., 2005. Tectonic geomorphology, drainage basin metrics, and active mountain fronts. Geografia Fisica e Dinamica Quaternaria 28 (1), 7–21.

Frankel, K.L., Pazzaglia, F.J., 2006. Mountain fronts, base-level fall, and landscape evolution: insights from the southern Rocky Mountains. Special Papers-Geol. Soc. Am. 398, 419.

Furque, G., González, P., Caballé, M., 1998. Descripción de la hoja geológica 3169-II, San José de Jáchal (Provincias de San Juan y La Rioja). Servício Geológico y Minero Argentino Boletín 259.

Gaidzik, K., Ramírez-Herrera, M.T., 2017. Geomorphic indices and relative tectonic uplift in the Guerrero sector of the Mexican forearc. Geosci. Front. 8 (4), 885–902.

Gao, M., Zeilinger, G., Xu, X., Wang, Q., Hao, M., 2013. DEM and GIS analysis of geomorphic indices for evaluating recent uplift of the northeastern margin of the Tibetan Plateau, China. Geomorphology 190, 61–72.

Giaconia, F., Booth-Rea, G., Martínez-Martínez, J.M., Azañón, J.M., Pérez-Peña, J.V., Pérez-Romero, J., Villegas, I., 2012. Geomorphic evidence of active tectonics in the Sierra Alhamilla (eastern Betics, SE Spain). Geomorphology 145, 90–106.

Giambiagi, L., Mescua, J., Bechis, F., Tassara, A., Hoke, G., 2012. Thrust belts of the southern Central Andes: along-strike variations in shortening, topography, crustal geometry, and denudation. Bulletin 124 (7–8), 1339–1351.

Groeber, P., 1944. Movimientos tectónicos contemporáneos y un nuevo tipo de dislocaciones. Universidad Nacional de La Plata, Notas del Museo de La Plata. Geologa 9, 263–375.

Guerrero, M., Lavandaio, E., Marcos, O., 1993. Mapa geológico de la provincia de La Rioja escala 1: 500,000. Dirección Nacional del Servicio Geológico, Secretaría de Minería República Argentina.

Gürbüz, A., Gürer, Ö.F., 2008. Tectonic geomorphology of the north Anatolian Fault zone in the lake Sapanca Basin (eastern Marmara Region, Turkey). Geosci. J. 12 (3), 215–225.

Gutscher, M.A., Spakman, W., Bijwaard, H., Engdahl, E.R., 2000. Geodynamics of flat subduction: seismicity and tomographic constraints from the Andean margin. Tectonics 19 (5), 814–833.

Harbor, D.J., 1997. Landscape evolution at the margin of the Basin and Range. Geology 25 (12), 1111–1114.

Harlin, J.M., 1978. Statistical moments of the hypsometric curve and its density function. J. Int. Assoc. Math. Geol. 10 (1), 59–72.

Houston, J., Hartley, A.J., 2003. The central Andean west-slope rainshadow and its potential contribution to the origin of hyper-aridity in the Atacama desert. Int. J. Climatol. 23 (12), 1453–1464.
Isacks, B.L., 1988. Uplift of the central Andean plateau and bending of the Bolivian orocline. J. Geophys. Res. Solid Earth 93 (B4), 3211–3231.
Jansen, J.D., Codilean, A.T., Bishop, P., Hoey, T.B., 2010. Scale dependence of lithological control on topography: bedrock channel geometry and catchment morphometry in western Scotland. J. Geol. 118 (3), 223–246.
Jordan, T.E., Allmendinger, R.W., 1986. The Sierras Pampeanas of Argentina: A modern analogue of Rocky Mountain foreland deformation. Am. J. Sci 286 (10), 737–764, http://dx.doi.org/10.2475/ajs.286.10.737.
Jordan, T.E., Gardeweg, M., 1989. Tectonic Evolution of the Late Cenozoic Central Andes (20–33 S). The Evolution of the Pacific Ocean Margins., pp. 193–207.
Jordan, T.E., Isacks, B.L., Allmendinger, R.W., Brewer, J.A., Ramos, V.A., Ando, C.J., 1983a. Andean tectonics related to geometry of subducted Nazca plate. Geol. Soc. Am. Bull. 94 (3), 341–361.
Jordan, T.E., Isacks, B., Ramos, V.A., Allmendinger, R.W., 1983b. Mountain building in the Central Andes. Episodes 557 (3), 20–26.
Jordan, T.E., Allmendinger, R.W., Damanti, J.F., Drake, R.E., 1993. Chronology of motion in a complete thrust belt: the Precordillera, 30-31 S, Andes Mountains. J. Geol. 101 (2), 135–156.
Kadinsky-Cade, K., Reilinger, R., Isacks, B., 1985. Surface deformation associated with the November 23, Caucete, Argentina, earthquake sequence. J. Geophys. Res. Solid Earth 90 (B14), 12691–12700.
Keen-Zebert, A., Hudson, M.R., Shepherd, S.L., Thaler, E.A., 2017. The effect of lithology on valley width, terrace distribution, and bedload provenance in a tectonically stable catchment with flat-lying stratigraphy. Earth Surf. Process. Landf. 42 (10), 1573–1587.
Keller, E., Pinter, N., 2002. Active tectonics: earthquakes, uplift, and landscape. Prentice Hall, Upper Saddle River, NJ.
Kendrick, E., Bevis, M., Smalley, R., Cifuentes, O., Galban, F., 1999. Current rates of convergence across the Central Andes: estimates from continuous GPS observations. Geophys. Res. Lett. 26, 541–544.
Kendrick, E., Bevis, M., Smalley, R., Brooks, B., 2001. An integrated crustal velocity field for the central Andes. Geochem. Geophys. Geosystems 2 (11).
Kendrick, E., Bevis, M., Smalley, R., Brooks, B., Vargas, R.B., Laurıa, E., Fortes, L.P.S., 2003. The Nazca–South America Euler vector and its rate of change. J. South Am. Earth Sci. 16 (2), 125–131.
Kendrick, E., Brooks, B.A., Bevis, M., Smalley, R., Lauria, E., Araujo, M., Parra, H., 2006. Active orogeny of the South-Central Andes studied with GPS geodesy. Revista de la Asociación Geológica Argentina 61 (4), 555–566.
Kirby, E., Whipple, K.X., 2012. Expression of active tectonics in erosional landscapes. J. Struct. Geol. 44, 54–75.
Kirby, E., Whipple, K.X., Tang, W., Chen, Z., 2003. Distribution of active rock uplift along the eastern margin of the Tibetan Plateau: inferences from bedrock channel longitudinal profiles. J. Geophys. Res. Solid Earth 108 (B4).
Kirkby, M.J., Carson, M.J., 1972. Hillslope Form and Process. Cambridge University Press, Cambridge.
Kley, J., Monaldi, C.R., 1998. Tectonic shortening and crustal thickness in the Central Andes: How good is the correlation? Geology 26 (8), 723–726.
Korup, O., 2008. Rock type leaves topographic signature in landslide-dominated mountain ranges. Geophys. Res. Lett. 35, L11402, http://dx.doi.org/10.1029/2008GL034157.
Kühni, A., Pfiffner, O.A., 2001. The relief of the Swiss Alps and adjacent areas and its relation to lithology and structure: topographic analysis from a 250-m DEM. Geomorphology 41 (4), 285–307.
Lague, D., Davy, P., Crave, A., 2000. Estimating uplift rate and erodibility from the area-slope relationship: examples from Brittany (France) and numerical modelling. Phys. Chem. Earth A 25, 543–548.
Lague, D., Crave, A., Davy, P., 2003. Laboratory experiments simulating the geomorphic response to tectonic uplift. J. Geophys. Res. Solid Earth 108 (B1).
Lara, G., Perucca, L., Rothis, M., Pantano, A., Sáez, M., 2018. Actividad tectónica cuaternaria del Sistema de Falla Maradona, Precordillera Central, Argentina. Andean Geol. 45 (2), 145–160.
Lifton, N.A., Chase, C.G., 1992. Tectonic, climatic and lithologic influences on landscape fractal dimension and hypsometry: implications for landscape evolution in the San Gabriel Mountains, California. Geomorphology 5 (1–2), 77–114.
McQuarrie, N., Horton, B.K., Zandt, G., Beck, S., DeCelles, P.G., 2005. Lithospheric evolution of the Andean fold–thrust belt, Bolivia, and the origin of the central Andean plateau. Tectonophysics 399 (1–4), 15–37.
Meigs, A., Krugh, W.C., Schiffman, C., Vergés, J., Ramos, V.A., 2006. Refolding of thin-skinned thrust sheets by active basement-involved thrust faults in the eastern Precordillera of western Argentina. Revista de la Asociación Geológica Argentina 61 (4), 589–603.
Millán, J.L., Perucca, L.P., 2011. Análisis neotectónico del extremo norte del sobrecorrimiento La Cantera, provincia de San Juan, Argentina. Rev. Mex. Cienc. Geolã³gicas 28 (3), 337–348.
Miró, R.C., Gaido, M.F., Candiani, J.C., Aimar, C., 2005. Hoja Geológica 2966-IV Recreo. Servicio Geológico Minero Argentino, Buenos Aires.
Moglen, G.E., Bras, R.L., 1995. The effect of spatial heterogeneities on geomorphic expression in a model of basin evolution. Water Resour. Res. 31 (10), 2613–2623.
Molnar, P., Anderson, R.S., Kier, G., Rose, J., 2006. Relationships among probability distributions of stream discharges in floods, climate, bed load transport, and river incision. J. Geophys. Res. Earth Surf. 111 (F2).
Mora, A., Gaona, T., Kley, J., Montoya, D., Parra, M., Quiroz, L.I., et al., 2009. The role of inherited extensional fault segmentation and linkage in contractional orogenesis: a reconstruction of Lower Cretaceous inverted rift basins in the Eastern Cordillera of Colombia. Basin Res. 21 (1), 111–137.
Mulcahy, P., Chen, C., Kay, S.M., Brown, L.D., Isacks, B.L., Sandvol, E., Heit, B., Yuan, X., Coira, B.L., 2014. Central Andean mantle and crustal seismicity beneath the Southern Puna plateau and the northern margin of the Chilean-Pampean flat slab. Tectonics 33 (8), 1636–1658.
Ortiz, G., Alvarado, P., Fosdick, J.C., Perucca, L., Saez, M., Venerdini, A., 2015. Active deformation in the northern Sierra de Valle Fértil, Sierras Pampeanas, Argentina. J. South Am. Earth Sci. 64, 339–350.
Ouchi, S., 34(6) 2002. Effects of Uplift on the Development of Experimental Erosion Landform: Geological Society of America Abstracts with Programs., pp. 129.
Özkaymak, Ç., 2015. Tectonic analysis of the Honaz Fault (western Anatolia) using geomorphic indices and the regional implications. Geodin. Acta 27 (2–3), 110–129.
Özkaymak, Ç., Sözbilir, H., 2012. Tectonic geomorphology of the Spildağı high ranges, western Anatolia. Geomorphology 173, 128–140.
Özsayın, E., 2016. Relative tectonic activity assessment of the Çameli Basin, Western Anatolia, using geomorphic indices. Geodin. Acta 28 (4), 241–253.
Pedrera, A., Pérez-Peña, J.V., Galindo-Zaldívar, J., Azañón, J.M., Azor, A., 2009. Testing the sensitivity of geomorphic indices in areas of low-rate active folding (eastern Betic Cordillera, Spain). Geomorphology 105 (3), 218–231.
Peel, M.C., Finlayson, B.L., McMahon, T.A., 2007. Updated world map of the Köppen-Geiger climate classification. Hydrol. Earth Syst. Sci. Discuss. 4 (2), 439–473.
Pérez-Peña, J.V., Azañón, J.M., Azor, A., 2009. CalHypso: An ArcGIS extension to calculate hypsometric curves and their statistical moments. Applications to drainage basin analysis in SE Spain. Comput. Geosci. 35 (6), 1214–1223.
Pérez-Peña, J.V., Azor, A., Azañón, J.M., Keller, E.A., 2010. Active tectonics in the Sierra Nevada (betic Cordillera, SE Spain): insights from geomorphic indexes and drainage pattern analysis. Geomorphology 119 (1-2), 74–87.
Perucca, L.P., Onorato, R., 2011. Fallas con actividad cuaternaria en el corredor tectónico Matagusanos-Maradona-Acequión entre los ríos de La Flecha y del Agua, provincia de San Juan. Revista de la Asociación Geológica Argentina 68 (1), 39–52.
Perucca, L., Rothis, M., Bezerra, F.H., Vargas, N., Lima, J., 2015. Late quaternary evolution of the La Cantera Fault System (Central Precordillera, Argentina): a morphotectonic and paleoseismic analysis. Tectonophysics 661, 200–209.
Peters, G., van Balen, R.T., 2007. Tectonic geomorphology of the northern Upper Rhine graben, Germany. Glob. Planet. Change 58 (1), 310–334.
Pilger, R.H., 1984. Cenozoic plate kinematics, subduction and magmatism: south American Andes. J. Geol. Soc. 141 (5), 793–802.
Ragona, D., Anselmi, G., Gonzalez, P., Vujovich, G., 1995. Mapa geológico de la provincia de San Juan escala 1: 500,000. Dirección Nacional del Servicio Geológico, Secretaría de Minería República Argentina.
Ramírez-Herrera, M.T., 1998. Geomorphic assessment of active tectonics in the Acambay Graben, Mexican volcanic belt. Earth Surf. Process. Landforms: J. Br. Geomorphol. Group 23 (4), 317–332.
Ramos, V.A., 1988. The tectonics 0f the Central Andes; 30 to 33 S latitude. In: Processes in continental lithospheric deformation., pp. 31.
Ramos, V.A., Folguera, A., 2009. Andean flat-slab subduction through time. Geol. Soc. London Spec. Publ. 327 (1), 31–54.
Ramos, V.A., Vujovich, G.I., 2000. Hoja geológica 3169-IV San Juan, Provincia de San Juan. Servicio Geológico Minero Argentino.
Ramos, V.A., Cegarra, M., Cristallini, E., 1996. Cenozoic tectonics of the High Andes of west-central Argentina (30–36 S latitude). Tectonophysics 259 (1-3), 185–200.
Ramos, V.A., Cegarra, M., Lo Forte, G., Cominguez, A., 1997. El frente orogénico en la Sierra de Pedernal (San Juan, Argentina): su migración a través de los depósitos orogénicos. 8o Congreso Geológico Chileno, Actas 3, 1709–1713.
Ramos, V.A., Dallmeyer, R.D., Vujovich, G., 1998. Time constraints on the Early Palaeozoic docking of the Precordillera, central Argentina. Geol. Soc. London Spec. Publ. 142 (1), 143–158.
Ramos, V., Caminos, R., Cortes, J.M., 2000. Hoja geológica 3369-I Cerro Aconcagua (1: 250.000). Subsecretaría de Minería de la Nación, Dirección Nacional del Servicio Geológico, Buenos Aires.
Ramos, V.A., Cristallini, E.O., Pérez, D.J., 2002. The Pampean flat-slab of the Central Andes. J. South Am. Earth Sci. 15 (1), 59–78.
Ramos, V.A., Zapata, T., Cristallini, E.O., 2004. The Andean thrust system: structural styles and orogenic shortening. In: McClay, K.R. (Ed.), Thrust Tectonics and Petroleum Systems: American Association of Petroleum Geologists Memoir. , p. 82.
Ramos, V.A., Aguirre-Urreta, M.B., Álvarez, P.P., Coluccia, A., Giambiagi, L., Pérez, D.J., et al., 2010. Hoja Geológica 3369-III Cerro Tupungato. Servicio Geológico Minero Argentino, Buenos Aires.
Regnier, M., Chatelain, J.L., Smalley Jr, R., Chiu, J.M., Isacks, B.L., Araujo, M., 1992. Seismotectonics of Sierra Pie de Palo, a basement block uplift in the Andean foreland of Argentina. Bull. Seismol. Soc. Am. 82 (6), 2549–2571.
Richardson, T., Ridgway, K.D., Gilbert, H., Martino, R., Enkelmann, E., Anderson, M., Alvarado, P., 2013. Neogene and Quaternary tectonics of the Eastern Sierras Pampeanas, Argentina: active intraplate deformation inboard of flat-slab subduction. Tectonics 32 (3), 780–796.
Rimando, J.M., Schoenbohm, L.M., Costa, C.H., Owen, L.A., Cesta, J.M., Richard, A.D., Gardini, C.E., 2019. Late Quaternary Activity of the La Rinconada Fault Zone, San Juan, Argentina. Tectonics 38 (3), 916–940.
Robl, J., Heberer, B., Prasicek, G., Neubauer, F., Hergarten, S., 2017. The topography of a continental indenter: the interplay between crustal deformation, erosion, and base level changes in the eastern Southern Alps. J. Geophys. Res. Earth Surf. 122 (1), 310–334.

Rockwell, T.K., Keller, E.A., Johnson, D.L., 1985. Tectonic geomorphology of alluvial fans and mountain fronts near Ventura, California. In: Morisawa, M. (Ed.), Tectonic Geomorphology. Proceedings of the 15th Annual Geomorphology Symposium. Allen and Unwin Publishers, Boston, pp. 183–207.
Rockwell, T.K., Ragona, D.E., Meigs, A.J., Owen, L.A., Costa, C.H., Ahumada, E.A., 2014. Inferring a Thrust-Related Earthquake History from Secondary Faulting: A Long Rupture Record of La Laja Fault, San Juan, Argentina. Bull. Seismol. Soc. Am. 1, 269–284.
Rothis, L.M., Perucca, L.P., Malnis, P.S., Zuñiga, A.P., Alcacer, J.M., Haro, F.M., Vargas, N., 2018. Morphotectonic analysis in the southwestern piedmont of the Andean foreland, Sierras Pampeanas Occidentales, San Juan, Argentina. Geosciences = Geociências 37 (1), 55–74.
Salomon, E., Schmidt, S., Hetzel, R., Mingorance, F., Hampel, A., 2013. Repeated folding during late Holocene earthquakes on the La Cal thrust fault near Mendoza city (Argentina). Bull. Seismol. Soc. Am. 103 (2A), 936–949.
Schmidt, S., Hetzel, R., Mingorance, F., Ramos, V.A., 2011. Coseismic displacements and Holocene slip rates for two active thrust faults at the mountain front of the Andean Precordillera (~ 33° S). Tectonics 30 (5).
Schoenbohm, L.M., Costa, C.H., Brooks, B.A., Bohon, W., Gardini, C., Cisneros, H., December 2013. Fault interaction along the Central Andean thrust front: the Las Peñas thrust, Cerro Salinas thrust and the Montecito anticline. AGU Fall Meeting Abstracts.
Schumm, S.A., 1956. Evolution of drainage systems and slopes in badlands at Perth Amboy, New Jersey. Geol. Soc. Am. Bull. 67 (5), 597–646.
Schumm, S.A., Parker, R.S., 1973. Implications of complex response of drainage systems for Quaternary alluvial stratigraphy. Nat. Phys. Sci. 243 (128), 99–100.
Selby, M.J., 1980. A rock mass strength classification for geomorphic purposes: with tests from Antarctica and New Zealand. Zeit. fur Geomorph., NF 24, 31–51.
Selim, H.H., Tüysüz, O., Karakaş, A., Taş, K.Ö., 2013. Morphotectonic evidence from the southern branch of the North Anatolian Fault (NAF) and basins of the south Marmara sub-region, NW Turkey. Quat. Int. 292, 176–192.
Sempere, T., Hérail, G., Oller, J., Bonhomme, M.G., 1990. Late Oligocene-early Miocene major tectonic crisis and related basins in Bolivia. Geology 18 (10), 946–949.
Sheffels, B.M., 1990. Lower bound on the amount of crustal shortening, in the central Bolivian Andes. Geology 18 (9), 812–815.
Siame, L.L., Bourlès, D.L., Sébrier, M., Bellier, O., Carlos Castano, J., Araujo, M., Perez, M., Raisbeck, G., Yiou, F., 1997. Cosmogenic dating ranging from 20 to 700 ka of a series of alluvial fan surfaces affected by the El Tigre fault, Argentina. Geology 25 (11), 975–978.
Siame, L.L., Bellier, O., Sébrier, M., Bourlès, D.L., Leturmy, P., Perez, M., Araujo, M., 2002. Seismic hazard reappraisal from combined structural geology, geomorphology and cosmic ray exposure dating analyses: the Eastern Precordillera thrust system (NW Argentina). Geophys. J. Int. 150 (1), 241–260.
Siame, L.L., Bellier, O., Sébrier, M., Araujo, M., 2005. Deformation partitioning in flat subduction setting: case of the Andean foreland of western Argentina (28°S–33°S). Tectonics 24 (5).
Siame, L., Bellier, O., Sébrier, M., 2006. Active tectonics in the Argentine Precordillera and Western Sierras Pampeanas. Rev. Asoc. Geol. Arg. 61 (4), 604–619.
Siame, L.L., Sébrier, M., Bellier, O., Bourlès, D., Costa, C., Ahumada, E.A., Gardini, C., Cisneros, H., 2015. Active basement uplift of Sierra Pie de Palo (Northwestern Argentina): rates and inception from10Be cosmogenic nuclide concentrations. Tectonics 34 (6), 1129–1153.
Silva, P.G., Goy, J.L., Zazo, C., Bardajı, T., 2003. Fault-generated mountain fronts in southeast Spain: geomorphologic assessment of tectonic and seismic activity. Geomorphology 50 (1), 203–225.
Smalley, R., Isacks, B.L., 1990. Seismotectonics of thin-and thick-skinned deformation in the Andean Foreland from local network data: evidence for a seismogenic lower crust. J. Geophys. Res. Solid Earth 95 (B8), 12487–12498.
Smalley, R., Pujol, J., Regnier, M., Chiu, J.M., Chatelain, J.L., Isacks, B.L., Araujo, M., Puebla, N., 1993. Basement seismicity beneath the Andean Precordillera thin-skinned thrust belt and implications for crustal and lithospheric behavior. Tectonics 12 (1), 63–76.
Snyder, N.P., Whipple, K.X., Tucker, G.E., Merritts, D.J., 2000. Landscape response to tectonic forcing: digital elevation model analysis of stream profiles in the Mendocino triple junction region, northern California. Geol. Soc. Am. Bull. 112 (8), 1250–1263.
Strahler, A.N., 1952. Hypsometric (area-altitude) analysis of erosional topography. Geol. Soc. Am. Bull. 63 (11), 1117–1142.
Suriano, J., Limarino, C.O., Tedesco, A.M., Alonso, M.S., 2015. Sedimentation model of piggyback basins: cenozoic examples of San Juan Precordillera, Argentina. Geol. Soc. London Spec. Publ. 399 (1), 221–244.
Telbisz, T., Kovács, G., Székely, B., Szabó, J., 2013. Topographic swath profile analysis: a generalization and sensitivity evaluation of a digital terrain analysis tool. Zeitschrift für Geomorphologie 57 (4), 485–513.
Tripaldi, A., Forman, S.L., 2007. Geomorphology and chronology of Late Quaternary dune fields of western Argentina. Palaeogeogr. Palaeoclimatol. Palaeoecol. 251 (2), 300–320.
Tucker, G.E., 2004. Drainage basin sensitivity to tectonic and climatic forcing: implications of a stochastic model for the role of entrainment and erosion thresholds. Earth Surf. Process. Landf. 29 (2), 185–205.
Uliarte, E., Bastías, H., Ruzycki, L., 1987. Morfología y neotectónica en el Cerro La Chilca, Pedernal, Provincia de San Juan, Argentina. 10° Congr Geol Argent Tucuman, Actas, 227–230, 1.
VanLaningham, S., Meigs, A., Goldfinger, C., 2006. The effects of rock uplift and rock resistance on river morphology in a subduction zone forearc, Oregon, USA. Earth Surf. Processes Landforms: J. Br. Geomorphol. Res. Group 31 (10), 1257–1279.
Vergés, J., Ramos, V.A., Meigs, A., Cristallini, E., Bettini, F.H., Cortés, J.M., 2007. Crustal wedging triggering recent deformation in the Andean thrust front between 31° S and 33° S: Sierras Pampeanas-Precordillera interaction. J. Geophys. Res. Solid Earth 112 (B3).
Viveen, W., Van Balen, R.T., Schoorl, J.M., Veldkamp, A., Temme, A.J.A.M., Vidal-Romani, J.R., 2012. Assessment of recent tectonic activity on the NW Iberian Atlantic Margin by means of geomorphic indices and field studies of the Lower Miño River terraces. Tectonophysics 544, 13–30.
Von Gosen, W., 1992. Structural evolution of the Argentine Precordillera: The Rio San Juan section. J. Struct. Geol. 14 (6), 643–667.
von Huene, R., Corvalán, J., Flueh, E.R., Hinz, K., Korstgard, J., Ranero, C.R., Weinrebe, W., 1997v. Tectonic control of the subducting Juan Fernández Ridge on the Andean margin near Valparaiso, Chile. Tectonics 16 (3), 474–488.
Vujovich, G., Chernicoff, J., Tchiliguirian, P., Godeas, M., Marín, G., Pezzutti, N., Sepúlveda, E., 1998. Hoja geológica 3166-III, Chepes, provincias de San Juan y La Rioja. Servicio Geológico Minero Argentino.
Walcott, R.C., Summerfield, M.A., 2008. Scale dependence of hypsometric integrals: an analysis of southeast African basins. Geomorphology 96 (1–2), 174–186.
Watkinson, I.M., Hall, R., 2017. Fault systems of the eastern Indonesian triple junction: evaluation of Quaternary activity and implications for seismic hazards. Geol. Soc. London Spec. Publ. 441 (1), 71–120.
Wells, S.G., Bullard, T.F., Menges, C.M., Drake, P.G., Karas, P.A., Kelson, K.I., Ritter, J.B., Wesling, J.R., 1988. Regional variations in tectonic geomorphology along a segmented convergent plate boundary pacific coast of Costa Rica. Geomorphology 1 (3), 239–265.
Wigger, P.J., Schmitz, M., Araneda, M., Asch, G., Baldzuhn, S., Giese, P., Heinsohn, W.-D., Martínez, E., Ricaldi, E., Rower, P., Viramonte, J., 1994. Variation in the crustal structure of the southern Central Andes deduced from seismic refraction investigations. In: Tectonics of the Southern Central Andes. Springer, Berlin, Heidelberg, pp. 23–48.
Wobus, C., Whipple, K.X., Kirby, E., Snyder, N., Johnson, J., Spyropolou, K., Crosby, B., Sheehan, D., Willett, S.D., 2006. Tectonics from topography: procedures, promise, and pitfalls. Special Papers-Geol. Soc. Am. 398, 55.
Yıldırım, C., 2014. Relative tectonic activity assessment of the Tuz Gölü fault zone; Central Anatolia, Turkey. Tectonophysics 630, 183–192.
Zandt, G., Velasco, A.A., Beck, S.L., 1994. Composition and thickness of the southern Altiplano crust, Bolivia. Geology 22 (11), 1003–1006.
Zapata, T.R., 1998. Crustal structure of the Andean thrust front at 30 S latitude from shallow and deep seismic reflection profiles, Argentina. J. South Am. Earth Sci. 11 (2), 131–151.
Zapata, T.R., Allmendinger, R.W., 1996. Thrust-front zone of the Precordillera, Argentina: a thick-skinned triangle zone. AAPG Bull. 80 (3), 359–381.